Challenge Journal of
CONCRETE RESEARCH LETTERS

Vol.12 No.3 (2021)

absorption acoustic emission artificial neural network compressive strength concrete corrosion cracking ductility durability energy absorption ferrocement flaky aggregate fly ash fracture mechanical properties mortar reinforced concrete self-compacting concrete silica fume strengthening superplasticizer tensile strength waste disposal water absorption w ility

ISSN 2548-0928

TULPAR ACADEMIC PUBLISHING

Challenge Journal of Concrete Research Letters

E-mail: *cjcrl@challengejournal.com*

Web page: *cjcrl.challengejournal.com*

TULPAR Academic Publishing
www.tulparpublishing.com

Challenge Journal of Concrete Research Letters

CONTENTS

Research Articles

TULPAR ACADEMIC PUBLISHING

Challenge Journal of Concrete Research Letters

Research Article

Predicting and comparing the fire performance of a small-scale composite structure

Burak Kaan Cirpici [a,*]

[a] *Department of Civil Engineering, Erzurum Technical University, 25050 Erzurum, Turkey*

ABSTRACT

The purpose of this paper is to investigate a strategy for the fire testing of reduced scale structural models which will help engineers design safer structures and reduce the loss from fires. The concept of this work is how composite frame floor arrangements, beam-column connections might be modelled at a small scale suitable for fire testing. Testing full-scale is expensive, besides the testing of scaled model produces reasonable results which help us to understand the failure mechanism and all significant thermo-structural responses involved in a fire. Thermal effects within a structural element generate fire curve, thermal input and structural displacement output, in other words cause and impact. Dimensional analysis, which is a condition for dynamic similarity between prototype and model, can be achieved when all the dimensionless groups are set equal for both model and prototype. On the other hand, scaling rules are used to decide how much insulating material will be used on a structure. 5-storey composite building with composite floors and steel columns has been modelled at small scale with 1/5. The obtained results from various parametric investigations show that the reduced scale model fire test method would be a feasible way to investigate the fire performance of composite structures.

ARTICLE INFO

Article history:
Received 26 February 2021
Revised 26 April 2021
Accepted 7 July 2021

Keywords:
Composite structures
Fire resistance
Fire protection
Steel temperatures
Modelling
Small-scale structures

1. Introduction

Structural models in other words reduced-scale structures sometimes called replica models have usually had an important role in structural engineering in terms of education, research and design. The physical modelling of a structure is an individual sample in which the model stands for a complete structure or some part of a structure. In other words, it is defined as any physical representation of a structure or assembly of structural elements, which is built by small scale compared with full size structures, is to be tested and the laws of resemblance must be applied to explain test results. However, it should be pointed out that the material of prototype can be used for the reduced–size structure. When these materials cannot be used for reduced–size structure, appropriate model materials must be taken place instead of prototype material and then the reduced–size structure is properly constituted a “model”.

In terms of fire tests on reduced scale models, as an alternative to the more traditional analysis methods, the use of reduced model tests analysis will be explored in this paper. Fire tests on small scale models offer considerable saving in costs and resources. Scaled experiments offer an economical alternative to full-scale tests. In other words, these tests are repetitive to find the parametric investigations easily and understanding the behaviour of structures and structural members of varying geometries, shapes and end conditions would be readily attainable. Structural models might be classified in different ways such as elastic, indirect, direct, strength, dynamic and other models (Harris and Sabnis, 1999). Chattaway et al. (1997) has described a procedure used in developing s small scale Class A fire threat (i.e. carbonaceous material such as wood, paper, etc.) by allowing easy scaling rules for the rate of a burning which is a function of surface area, temperature and other well-defined parameters. A methodology for the fire testing of

* *Corresponding author*. Tel.: 444-5-388 ; Fax: +90-442-230-0036 ; E-mail address: burak.cirpici@erzurum.edu.tr (B. K. Cirpici)
ISSN: 2548-0928 / DOI: https://doi.org/10.20528/cjcrl.2021.03.001

reduced scale structural model has been presented by O'connor et al. (1997) by applying the scale modelling principles to both structural testing and thermal modelling. In their model, steel and concrete columns, brickwork compartment walls and reinforced concrete floor slabs are used to apply the scaling methodology in standard fire condition. A water mist extinguishment design has been developed by Quintiere et al. (2007) using a quarter-scale model emphasizing scaling of flame radiation by varying the fuel radiative absorption coefficient. Cutter et al. (2009) have been proposed a new method for fire resistance testing of composite materials by developing composite panels subjected to combined fire and mechanical load in small scale. Radzi et al. (2016) has reviewed the complies methodologies, issues and challenges regarding small-scale fire tests on tunnel lining concrete including furnace tests on specimens of actual and reduced dimensions and the effects of loading, size reduction. Fire tests to cables at reduced scale have been performed by Girardin et al. (2016) only considering the external sheeting/jacket. Müllerová (2016) created a representative model of complete 3D structure model by reducing the time equation, energy equation, the border area and the fuel source through dimensionless groups. Krajčír and Müllerová (2017a, 2017b) have performed real 3D experiments in small-scale model representing the full-scale model in the effective way by exact calculation for suitable materials to represent real walls with certain thickness and fire resistance including wood cribs to represent the interior. A scaling method based on Froude scaling for the static fires has been examined by representing a gas burner, liquid pool, wood crib and polyurethane foam block (Quintiere et al., 2017). Bjørge et al. (2017) has aimed to develop a test concept for testing fire resistance of equipment protected with only air-gap and thermal insulation by demonstrating a conceptual methodology for small scale fire testing. Lannon et al. (2018) has followed a procedure based on gram-scale and/or milligram-scale standard testing to obtain relevant material properties which were employed to simulate the early stages of the room corner test, which was selected to represent the full-scale material performance. Wilson (2018) has developed numerical simulation of small-scale and full-scale fire experiments by firstly preparing a small-scale test apparatus for performing cone calorimeter test with a finite difference model and a CFD model. The compared results of this study show that 1D numerical model is not appropriate for the experimental configuration and heat transfer phenomena is found to be over-predicted through the non-degrading structural sections.

Based on the literature related to the scale modelling of fire tests, 5-story composite building involving composite floor systems and steel columns has been modelled at small scale with 1/5. The obtained results showed that choosing suitable scale factors for both structural elements' and insulation thermal properties including dimensions would reflect the similar behaviour with the full-scale.

2. Scale Modelling of Structures and Design Review Stage

The development of structural scaling introduces simple scaling rules to design the structural geometry, structural loading and boundary conditions. Every structural model must be designed due to the many similitude requirements that mean like connection between the model and the prototype structure. The theory of modelling relates to these similitude requirements which might be derived from a dimensional analysis (O'Connor and Silcock, 1992).

2.1. Theoretical development of structural scaling

Dimensional analysis will be used to develop the scale relations between important parameters which are involved in fire. In this study, "∼" will be used to define the dimensional equality and "^" will be used to define the dimensionless variables. In other words, dimensionless variables will be showed as a ratio of the variables e.g. $\hat{T} = T/T_{\infty}$, $\hat{\rho} = \rho/\rho_w$ and $\hat{t} = t/t_r$ show the dimensionless of temperature, density and time respectively. 's' is the scale factor or called the geometric length scale. In this work, the scale factor 's' is considered as 1/5. The reason is not only to adopt a model size which can be used in fire tests using a fire oven but also to provide the heat transfer phenomenon in a correct way in terms of size. The required equations for structural scaling have been taken from Wang (2006).

If an object is subjected to a fire, the change of temperature can be related to the heat flux onto object;

$$mc\frac{dT}{dt} \sim \dot{q} \tag{1}$$

where c and $\dot{q}$ represents the specific heat capacity and heat flux respectively. Herein, m is the mass which is related to density and volume of the object. As density's dimensionless factor is $\rho \sim s^0$, the dimensionless factor of mass is completely related to the dimensionless factor of volume as $m, V \sim s^3$ when the object is scaled by geometrically.

The heat generation rate and heat loss rate are scaled as;

$$\dot{Q} \sim s^{5/2} \tag{2}$$

$$\dot{q} \sim s^{5/2} \tag{3}$$

Since the same material is used in the small-scale models, the dimensional equality for c will be $c \sim s^0$. Hence Eq. (1) can be rewritten as;

$$s^3 s^0 \frac{dT}{dt} \sim s^{5/2} \tag{4}$$

where the temperature is independent from scale rules while the time scale can be invented as;

$$t \sim s^{1/2} \tag{5}$$

The structural scaling rule can be derived from the relevant equations, and the stress in one-dimensional form of structural member is used providing that there is no loss of generalization.

$$\varepsilon = \frac{\partial v}{\partial x} \tag{6}$$

where v is a deformation vector in x-direction and it is scaled like $v \sim s$, the scaled of strain will be $\varepsilon \sim s^0$. This corresponds that the strain value between prototype and model is a constant.

Stress may be related to force or strain as;

$$\sigma = \varepsilon E = \frac{\partial F}{\partial x \partial y} \tag{7}$$

Herein, elastic modulus (E), stress (σ) and force (F) are scaled by;

$$\sigma \sim s^0 \; and \; F \sim s^2 \tag{8}$$

If a beam-column model can be modelled as Fig. 1, the bending resistance and external moment may be written as;

$$-EI\frac{d^2y}{dx^2} = Py + M_1 + (M_2 - M_1)\frac{x}{L} \tag{9}$$

where y is the transverse deflection, E is the elastic modulus, and P is the axial force which occurred from the elevated temperature of the beam. M is the applied moment and L is the length of the beam. The deflection shape, which is shown in Fig. 1, should be similar to that of prototype providing that $dy/dx \sim s^0$. If the model is geometrically scaled ($x \sim s$), the scaling factor for transverse deflection will be ($y \sim s$).

Eq. (9) can be rewritten considering the geometrically scaling as;

$$-I\frac{d^2y}{dx^2} = Py + M_1 + (M_2 - M_1)\frac{x}{L} \tag{10}$$

As can be worked out from Eq. (10) that, the scale factor for force and moment are $P \sim s^2$ and $M \sim s^3$.

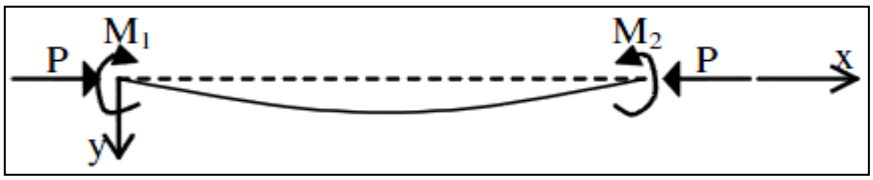

Fig. 1. Beam-column model (Wang, 2006).

When the same material is used for prototype and model, all those scaling rules can be summarized in Table 1.

Table 1. Summary of scale factor for structural scaling.

Quantities	Scale Factor
Length, L	s
Mass, m	s^3
Density, ρ	s^0
Heat generation rate, $\dot{Q}$	$s^{5/2}$
Heat loss rate, $\dot{q}$	$s^{5/2}$
Temperature, θ or T	s^0
Time, t	$s^{1/2}$
Strain, ε	s^0
Stress, σ	s^0
Elastic modulus, E	s^0
Force, F or P	s^2
Deformation, v	s
Area, A	s^2
Volume, V	s^3
Moment of inertia, I	s^4
Moment, M	s^3
Axial stiffness, K	s

2.2. Theoretical development of insulation scaling

After theoretical development of structural scaling, insulation for fire protection must be scaled due to the heat transfer through solids in compartment fires. Under these conditions, the equation can be shown as (Wang et al., 2008);

$$m_s c_s \frac{dT_s}{dt} + m_i c_i \frac{dT_i}{dt} \sim \frac{k_i}{\delta_i} A_s \left(T_f - T_s\right) \tag{11}$$

where s and i represent the structural materials and insulation respectively.

The structural materials (e.g. steel) and the insulation store the heat. The thermal conductivity of steel is higher than that in the insulation. Hence, the temperature may be considered as uniform in steel. On the other hand, there can be a simple assumption that the surface temperature of the insulation is equal to the hot gas temperature since thermal resistances of radiation and convection are small at the solid boundaries. Therefore, they are ignored in this study. To calculate the thickness of insulation in a small-scale model, Eq. (11) must be scaled with different scales. There are also different scaling approaches which can be derived depending on the heat capacity of insulation (Wang, 2006).

If the heat capacity of insulation is too important, the insulation properties can be obtained from Eq. (11) for scaled model by using dimensionless ratios. Using the insulation term, the scale modeling of insulation thickness must be $\delta_i \sim s^{1/4}$ (Wang, 2006).

Insulation materials are usually light-weight compared to the structural materials. Hence, the heat capacity of insulation may be ignored where the insulation thickness is thin. If the heat capacity is ignored, the scale modelling of insulation thickness is $\delta_i \sim s^{-1/2}$. The scaling rules for the design of wood cribs, fire compartment, insulation and structure considered in the paper are shown in Table 2. The fire compartment and the structure are both geometrically scaled, and the time is again scaled according to $t \sim s^{1/2}$.

3. Composite Beam Design and Modelling in Fire

3.1. Design of full-scaled composite beams

The calculations for full-scaled composite beams in terms of secondary and primary have been done and the section and insulation thicknesses have been determined by self-developed Fire Excel sheets. Plasterboard is considered as a protection material for full-scaled composite beams. The protected steel temperature has been checked against the critical temperature depending on the thickness of insulation. The standard fire is considered in the design of composite beams. Fire compartment is defined in terms of floor area, average windows height on all walls and total area of vertical opening and enclosure. The considered fire resistance time is 90 minutes. The design specifications such as insulation thickness and selected sections for beams can be shown in Table 3. Fig. 2 shows the protected and unprotected steel temperatures of the primary and secondary beam types under the Standard (ISO) fire condition (ISO, 2014).

Table 2. Scaling rules for fire, insulation and structures.

Design parameters	Scaling rules
Scaling rules for fuel design wood cribs	
Thickness of wood sticks, b_c	$s^{1/3}$
Spacing between wood sticks, s_c	$s^{1/3}$
Length of wood sticks, L_c	$s^{7/6}$
Number of layers, N_c	$s^{1/3}$
Number of wood stick per layer, n_c	$s^{5/6}$
Scaling rules for compartment design	
Wall material, k_w and ρ_w	$s^{3/2}$
Thickness of wall, δ_w	$s^{1/4}\left(\frac{k_w}{\rho_w c_w}\right)^{1/2}$
Scaling rules for insulation on steel structures	
Properties of insulation, k_i and ρ_i	s^0
Thickness of insulation, δ_i	$s^{-1/2}$
Scaling rules for structures	
Structural loadings, P and M	$P \sim s^2$, $M \sim s^3$
Boundary constrain, K	s

Table 3. Design specifications of full-scaled composite beams.

Design Specification	Primary Beam	Secondary Beam
Selected section	UB 305×165×54	UB 305×102×28
Design load in fire (kN/m), q_{fi}	42	21
Critical temperature (°C)	646.2	652.4
Fire resistance time for unprotected steel (min), t	15.6	12.38
Protected steel temperature for 90 min (°C)	542.8	592.6
Properties of fire protection material		
Material	Plasterboard	Plasterboard
Thickness (mm) $(d_p \sim s^{1/2})$	20	25

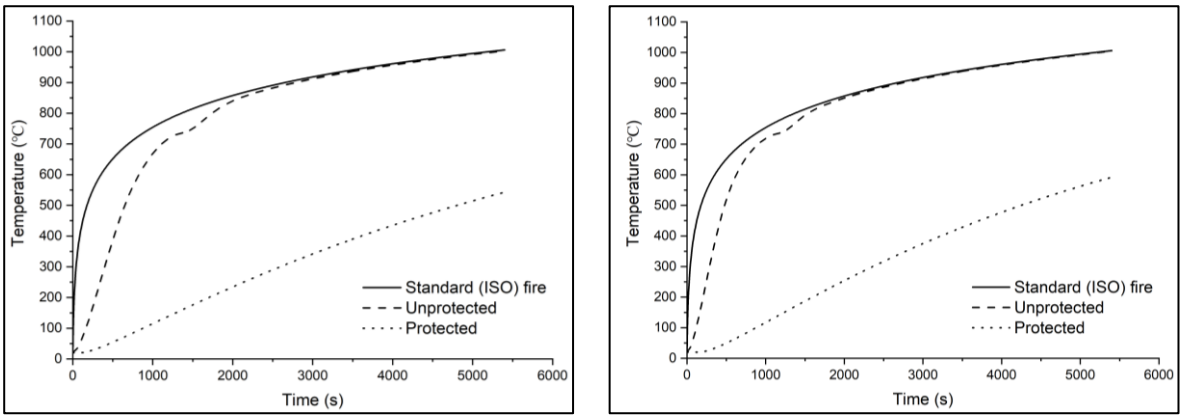

Fig. 2. Temperature distributions on full-scale primary beams and secondary beams.

3.2. Design of small-scaled composite beams

The design of composite beams at 1/5th-scale ($s = 1/5$) follows the same procedure as design of full-scaled. However, the design loads are estimated from the resistance bending moment of the small-scaled section. It can be seen after all calculations that the loads for prototype (real-structure) are lower than that loads for model. Hence, it should be put more weights or loads (additional) on 1/5-scale model such as sand bags to obtain the same deflection under fire conditions. Moreover, wood cribs have also their self-weight leads to an additional load. Thus, the loads, which have been applied in the design of real structure, will increase in the design of model. After calculating the primary and variable loads, critical temperatures can be estimated, and the resistance time can be modelled according to the time modelling rules. Besides, the thickness of protection must be modelled according to the rules of insulation scaling. Section properties of reduced scale model are worked out from geometrically modeling. The outputs from the developed model are shown in Table 4 in terms of section sizes, fire resistance time for unprotected steel and thickness of fire protection material. Fig. 3 shows the protected and unprotected primary and secondary beams at small scale. Without applying fire protection, primary beams can resist for 7 min against fire whereas this duration is 6.54 minutes for secondary beams due to their section area. Another outcome is those fire resistance times is almost half of the fire resistance times shown in Fig. 2 and Table 3 for full scale though there is no time scaling for the model.

Table 4. Design specifications of small-scaled composite beams.

Design Specification	Primary Beam	Secondary Beam
Selected section	UB 61×33×10.8	UB 61×20.4×5.6
Design load in fire (kN/m), q_{fi}	10.464	5.232
Critical temperature (°C)	608.3	620.83
Fire resistance time for unprotected steel (min), t	7	6.54
Properties of fire protection material		
Material	Plasterboard	Plasterboard
Thickness (mm) $(d_p \sim s^{1/2})$	45	56

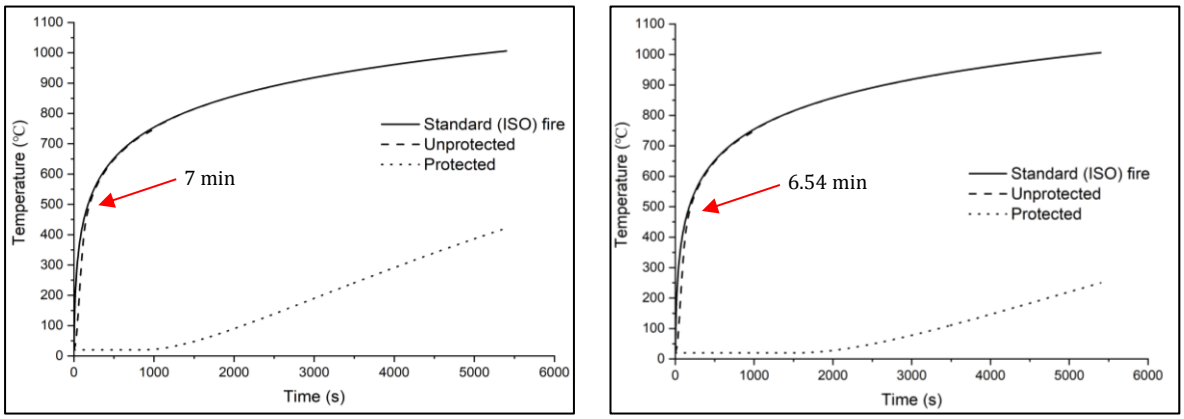

Fig. 3. Temperature distributions on small-scale primary beams and secondary beams.

4. Composite Slab Design and Modelling in Fire

4.1. Design of full-scaled composite slab

Firstly, the loads for full-scaled composite slab have been determined in terms of steel sheet load, concrete and finishes as the permanent loads and variable loads. Suitable steel decking has been chosen from Corus (Corus Pmf Comflor 51) (International, 2007). Effective thickness of the composite slab has been found based on steel decking properties using effective thickness method. After the determination of the effective thickness, design loads at ambient temperature has been calculated to estimate the design moments in terms of sagging moment at span (M_{sag}) and hogging moment at mid-support (M_{hog}). However, applied sagging and hogging moments depend on the reduction factor related to the load combination factor $(\psi_{1,1})$. On the other hand, there is a limitation for steel sheet profile which needs to be checked according to EC4, Part 1.2, Annex D, Section D.5 (CEN, 2005b). This necessary check is shown below in Fig. 4.

The results of design at fire situation and ultimate limit state design at ambient temperature can be shown in Table 5. After all design calculations, this stage is to work out the fire resistance according to the thermal insulation criterion. As fire compartment, it is considered externally fully glazed over 3.0 m from floor to ceiling

height. Fire resistance time is considered as 90 minutes for this building. The temperature of rebars and the parts of steel decking such as lower flange, web and upper flange, and compressive resistance of concrete and plastic moment resistance of slab have been calculated. Sagging moment resistance of slab should be compared with the design sagging moment. The calculation for hogging moment resistance follows the same procedure. However, the difference comes from using tension bar.

Scope of application

EC4, Part 1.2, Annex D, Section D.5

Field of application		Actual values			
Re-entrant steel sheet profiles	Trapezoidal steel sheet profiles				
70 mm ≤ l_1 ≤ 135 mm	80 mm ≤ l_1 ≤ 155 mm	l_1 =	112.5	mm	[OK]
110 mm ≤ l_2 ≤ 150 mm	32 mm ≤ l_2 ≤ 132 mm	l_2 =	137.5	mm	[OK]
38.5 mm ≤ l_3 ≤ 97.5 mm	40 mm ≤ l_3 ≤ 115 mm	l_3 =	40	mm	[OK]
50 mm ≤ h_1 ≤ 130 mm	50 mm ≤ h_1 ≤ 125 mm	h_1 =	79	mm	[OK]
30 mm ≤ h_2 ≤ 60 mm	50 mm ≤ h_2 ≤ 100 mm	h_2 =	51	mm	[OK]

[The slab is WITHIN the scope of application]

Fig. 4. Scope of application using developed EXCEL spreadsheet.

Table 5. Design specifications of small-scaled composite beams.

Design Specification	
Characteristic floor loading	Permanent Loads: Steel sheet, $G_{p,k} = 0.20\ kN/m^2$ Concrete, $G_{c,k} = 2.80\ kN/m^2$ Finishes, $G_{f,k} = 1.00\ kN/m^2$ Variable Loads: Live load, $Q_{k,l} = 5.00\ kN/m^2$
Material properties	Steel Sheet: Yield stress: $f_{p,y} = 255\ N/m^2$ Geometry of cross section, $h_1 = 79\ mm$ Thickness, $t_p = 0.7\ mm$ Cross-sectional area, $A_p = 1296.8\ mm^2/m$ Concrete: Type, light-weight $f_{c,k} = 30\ N/mm^2$ Height, $h_c = 130\ mm$ Cross-sectional area, $A_c = 120803.3\ mm^2/m$
Effective thickness of slab (mm), h_{eff}	120.8
Ultimate limit state design at ambient temperature (kNm/m)	$M_{sag} = 32.51$ $M_{hog} = 58.05$
Design at fire situation (kNm/m)	$M_{fi,Sd,sag} = 16.4$ $M_{fi,Sd,hog} = 29.3$
Sagging Moment Resistance of Slab	
Considered standard fire resistance time (min), R	90
Fire resistance time of slab (min), t_i	128.2
Sagging moment resistance (kNm/m)	$M_{fi,Rd,sag} = 43.3 > M_{fi,Sd,sag} = 16.8$ The composite slab is 'Satisfactory' against sagging moment
Hogging Moment Resistance of Slab	
Rebar diameter(mm), Φ	20
Tension bar cover, c	30
Normal force in hogging rebar, N_s (kN)	245.4
Hogging moment resistance (kNm/m)	$M_{fi,Rd,hog} = 77.3 > M_{fi,Sd,hog} = 29.2$ Satisfactory

4.2. Design of small-scaled composite slab

The response of compressive load is more important for any model concrete because the main property of concrete as a structural material is to carry the compression loads. The behaviour of prototype concrete under compression can be seen in a model concrete. Model concrete mixes must be designed properly and carefully to represent not only the tensile strength, time dependent behaviour but also the strength and the strain-stress relation under compression. In terms of materials included in model concrete mix, the cement is the same material in both prototype and model, but aggregates are different. For the model aggregates, ordinary well-graded concrete sand and sometimes fine crushed stone or pea gravel for larger-scale models are used with scaling of the particles. 'The finer particles in the model mix are limited to less than 10% passing the U.S. No. 100 sieve (0.149 mm mesh)' (Harris and Sabnis, 1999). The amount of aggregate, which is used in concrete mix, has a significant effect on the mechanical properties of model concrete.

A study about the influence of particle size distribution, shape and texture of the sand in micro concrete confirmed the earlier findings (Wijayasri, 1983).

The modelling of composite slab, the micro concrete can be used for concrete part. For the reinforcement part, to select and model the correct reinforcement for a concrete scaled model is the single and the most important step in the all process of modelling. For this modelling of composite slab, Black annealed wire can be considered as model reinforcement. Micro-concrete models may be reinforced with black annealed wire which can be found in the form of rolls. The wire is cold-drawn and annealed in the special factory. Before used in the models, it must be straightened by pulling. Hence this process strains the wire sufficiently to destroy the yield point. Stress-strain curve of prototype reinforcing steel should be chosen according to the reinforcing steel behaviour based on shape, diameter and their treatment under temperature conditions (Harris and Sabnis, 1999).

If the composite slab is modelled at 1/5-scale, the overall floor zone will be 150 mm including raised floor, slab, beam and services such as ceiling and lighting. The drawing for reduced-scale composite slab model can be shown in Fig. 5.

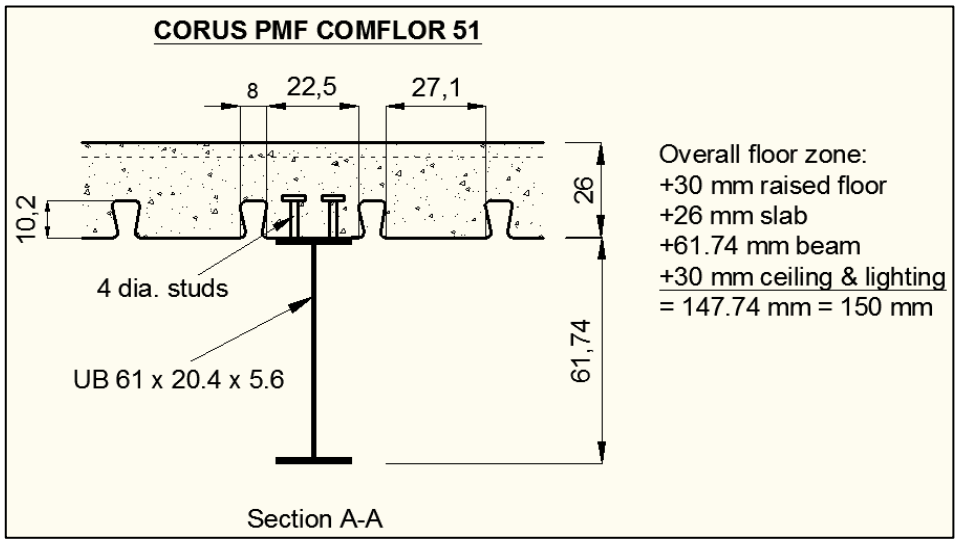

Fig. 5. The specifications of reduced scale composite beam and slab.

4.3. Design of wood cribs

A typical office fuel load is generally between 20 kg/m^2 and 60 kg/m^2 (Wang et al., 2007) and this fire loading condition should be scaled according to the heat loss and generation rate presented in Table 1. In the design of wood cribs, 40 kg/m^2 and 36 m^2 is assumed as the fuel load for a typical floor and floor area respectively. Therefore, the burning rate would be as,

$$m \approx \frac{m}{t} = \frac{40\ kg/m^2 \times\ 36\ m^2}{120\ min \times\ 60\ s/min} = 0.20\ kg/s$$

The average burning rate is scaled according to the $m \sim s^{5/2}$. Hence, the burning rate of the fuel for the 1/5-scale is approximately 3.58 g/s and the burning time in the scaled model would be 53.7 minutes. Wood cribs are thought to be designed from pine whose density is 530 kg/m^3. The total mass of the fuel load for a wood crib is calculated as,

$$3.58\ g/s \times 53.7\ min \times 60\ s/min = 11.53\ kg = 0.11\ kN$$

If this load converts into the uniform distributed load, it will be an additional load of 0.08 kN/m^2 per wood crib to the design of composite beam. Wood sticks have been designed as square cross-sections and scaled according to the scaling rules shown in Table 1. The design specifications can be given below in Table 6. Small-scaled wood crib model can be shown in Fig. 6.

Table 6. Design parameters of wood cribs.

Design Specification				
Scale	N_c	n_c	b_c (mm)	L_c (mm)
1	5	24	19.1	800
1/5	3	6	11	122

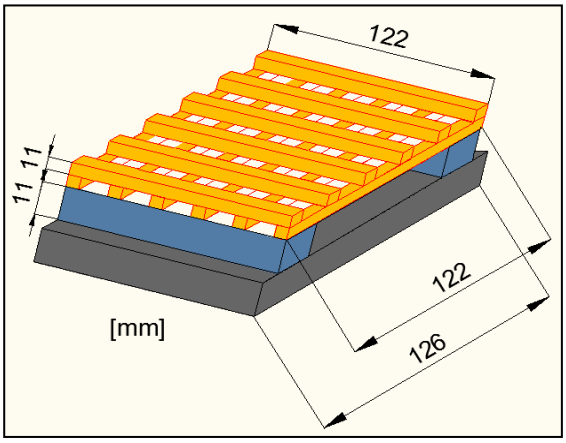

Fig. 6. Configuration of wood cribs.

5. Steel Column Design and Modelling in Fire

The very first important issue, which needs to be considered carefully, is the buckling resistance of column sections depending on the total design axial load. This loading changes based on the column position for instance edge, corner and internal. Columns are expected to be stable with or without fire protection under fire conditions. The section classification according to the web and flange design has been done based on Eurocode 3 Table 5.2 (CEN, 2005a).

5.1. Design of full-scaled steel columns in fire

The loading conditions, floor and column sizes, and material properties are assumed to be identical for all type of columns in terms of internal, edge and corner. These properties are shown in Table 7.

All columns are protected by box protection and their properties are shown in Table 8.

5.1.1. Design of internal columns

Internal columns carry the maximum load compared to the corner and edge columns. The design of columns under fire condition follows the similar procedure with beam design. However, they should be checked against the ultimate limit state design at ambient temperature whether they will satisfy the lateral torsional buckling. Therefore, ultimate limit state design check at ambient temperature and design check at room temperature have been performed herein this study. The design specifications of full-scaled internal columns in fire are shown in Table 9.

After checking the buckling resistance of the section, the column can be designed at fire situation. Design loading condition is compared against the buckling resistance at time t with uniform temperature. For the fire compartment, it is considered externally fully glazed over 3.0 m from floor to ceiling height as sketched in Fig. 7.

The properties of the fire compartment have been presented in Table 10.

Table 7. The considered properties of columns and floors.

General Specifications of Columns	
Characteristic of floor loading	$G_k = 4$ kN/m^2 $Q_k = 5.0$ kN/m^2
Floor and column sizes	Span B = 6 m, Span L = 6 m Column height = 4 m
Material Properties	Steel grade, $f_y = 275\ N/mm^2$ Elastic modulus, $E = 210000\ N/mm^2$

Table 8. Insulation properties of full-scaled columns.

Properties of Protection Material	Internal	Edge	Corner
Material	Plaster finish box protection	Plaster finish box protection	Plaster finish box protection
Thickness, d_p	25 mm	30 mm	35 mm
Density, ρ_p	1300 kg/m^3	1300 kg/m^3	1300 kg/m^3
Specific heat, c_p	1000 J/kg°K	1000 J/kg°K	1000 J/kg°K
Thermal conductivity, λ_p	0.50 W/m°K	0.50 W/m°K	0.50 W/m°K

Table 9. Design of full-scaled steel internal columns under fire condition.

Design Specifications of Internal Columns	
Selected section	UC 254×254×132
Floor area	36 m²
Section classification	Web, d/s = 15.6 (Section is Class 1) Flange, $b/2t$ = 6.31 (Section is Class 1)
Ultimate limit state design at ambient temperature	Partial factor, γ_G = 1.35 and $\gamma_{Q,1}$ = 1.5 Design loads, G_d = 194.4 kN/m Q_d = 270.0 kN/m One floor total load = 464.4 kN Number of floors = 5 Design load from upper 4 floors = 1857.6 kN Extra factored dead load (cladding, etc.) = 45 kN Total design axial compression load, N_{sd} = 2367.0 kN
Design at room temperature	Buckling resistance, $N_{b,Rd}$ = 3381.84 kN $N_{b,Rd} > N_{sd}$ (OK)

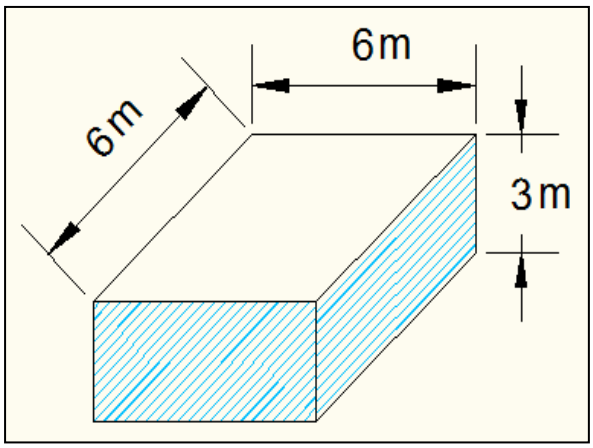

Fig. 7. Sketch of fire compartment.

Table 10. Fire compartment properties.

Opening and Enclosure	
Floor area, A_f	36.0 m²
Total vertical opening, A_v	18.0 m²
Average of windows height on all walls, h_{eq}	3.0 m
Total area of enclosure, A_t	168.0 m²
Density of wall material, ρ_w	1600 kg/m³
Specific heat, c_w	840 J/kg°K

The standard fire is considered herein this study and the steel temperature is around 990.2°C while maximum temperature is 1049.0°C after applying box protection for 90 minutes. The buckling resistance $(N_{bi,fi,t,Rd})$ at time t with uniform θ_a is 3361.5 kN while design loading in fire $(N_{fi,sd})$ is 1192.74 kN. Since buckling resistance is greater than the design loading, these internal columns can resist for 90 minutes under fire condition. The steel temperatures have been presented in Fig. 8 with and without insulation.

5.1.2. Design of edge columns

The same procedure applied in the previous section for the design of internal columns has been applied to the design of edge columns. With the aid of developed fire excel spread sheets, the summary of the sections' properties can be shown in Table 11.

The same fire compartment properties shown in Table 10 has been used herein for edge columns. Edge columns has also been protected by box protection of which thickness is 10 mm. After 90 minutes' box protection, the steel temperature reaches to 994.6°C whereas the maximum temperature is 1049.0°C. The buckling resistance of edge columns $(N_{bi,fi,t,Rd})$ at time t with uniform θ_a is 1972.5 kN while design loading in fire $(N_{fi,sd})$ is 607.7 kN. The buckling resistance is also greater than the design loading in fire. Therefore, these edge columns can resist for 90 minutes under standard fire condition. Fig. 9 shows the protected and unprotected temperature distribution on edge columns.

5.1.3. Design of corner columns

For the corner columns in the real structure, floor area and axial compression load changes. However, the considered loads in terms of permanent and variable and the material properties are identical with the internal and edge columns. The design specifications are shown in Table 12. These columns have also been protected by box protection to resist against 90 minutes' fire. The predicted steel temperature is 999.2°C and the maximum temperature is 1049.0°C. For the buckling resistance check, the buckling resistance $(N_{bi,fi,t,Rd})$ at time t with uniform θ_a is 1142.2 kN whereas design loading in fire $(N_{fi,sd})$ is 315.2 kN. Hence, the corner columns can resist against fire for 90 minutes.

The temperature profiles for both protected and unprotected corner columns are given in Fig. 10.

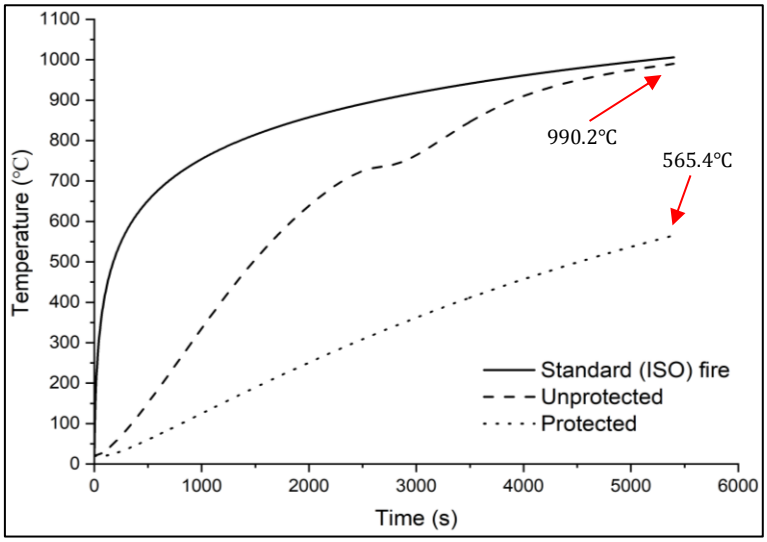

Fig. 8. Temperature distribution for internal columns.

Table 11. Design of full-scaled edge columns under fire condition.

Design Specifications of Edge Columns	
Selected section	UC 203×203×86
Floor area	18 m²
Section classification	Web, d/s = 12.7 (Section is Class 1) Flange, $b/2t$ = 5.1 (Section is Class 1)
Ultimate limit state design at ambient temperature	Partial factor, γ_G = 1.35 and $\gamma_{Q,1}$ = 1.5 Design loads, G_d = 97.2 kN/m Q_d = 135.0 kN/m One floor total load = 232.2 kN Number of floors = 5 Design load from upper 4 floors = 928.8 kN Extra factored dead load (cladding, etc.) = 45 kN Total design axial compression load, N_{sd} = 1206.0 kN
Design at room temperature	Buckling resistance, $N_{b,Rd}$ = 1881.53 kN $N_{b,Rd} > N_{sd}$ (OK)

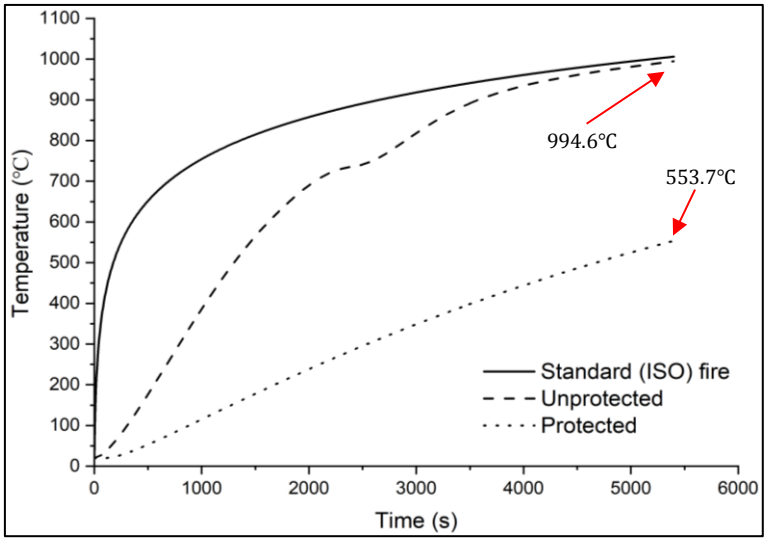

Fig. 9. Temperature distribution for edge columns.

Table 12. Design of full-scaled corner columns under fire condition.

Design Specifications of Corner Columns	
Selected section	UC 203×203×52
Floor area	9 m²
Section classification	Web, d/s = 12.7 (Section is Class 1) Flange, $b/2t$ = 5.1 (Section is Class 1)
Ultimate limit state design at ambient temperature	Partial factor, γ_G = 1.35 and $\gamma_{Q,1}$ = 1.5 Design loads, G_d = 948.6 kN/m Q_d = 67.5 kN/m One floor total load = 116.1 kN Number of floors = 5 Design load from upper 4 floors = 464.4 kN Extra factored dead load (cladding, etc.) = 45 kN Total design axial compression load, N_{sd} = 625.5 kN
Design at room temperature	Buckling resistance, $N_{b,Rd}$ = 1105.17 kN $N_{b,Rd} > N_{sd}$ (OK)

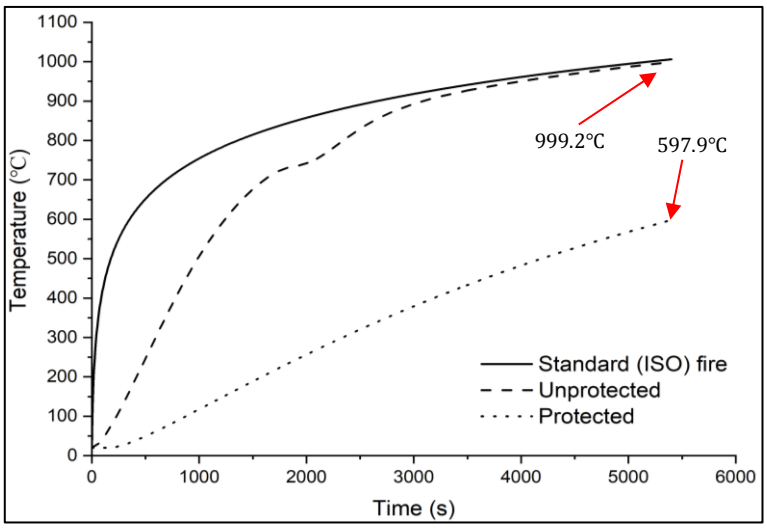

Fig. 10. Temperature distribution for corner columns.

5.2. Design of small-scaled columns in fire

All type of columns (internal, edge and corner) have been modelled at 1/5-scale. However, axial compression load has been worked out depending on the characteristic floor loading of composite floor. The section properties can be shown in Table 13.

The characteristic floor loading, floor and column sizes and material properties are identical for all type of columns. They have been also scaled according to the scaling rules with a scaler of 1/5. They are presented in Table 14.

The insulation properties of small scaled columns are identical with the prototype. However, the thickness of the box protection has been scaled according to the scaling rule presented in Table 2. The scaled properties of the box protection are shown in Table 15.

5.2.1. Design of small-scaled internal columns

The estimations of the compression load for all type of columns have been performed by using MATLAB. The same procedure in terms of buckling resistance check implies herein though. The summary of modelling of internal columns is shown in Table 16.

As can be seen from Table 16, the total design axial compression load (N_{sd}) is 130.8 kN while this load for the prototype was 2367.0 kN. This can be concluded that the load is not proportional with the scaling factor ($P \sim s^2$). However, the loads on the composite floor have been increased to prevail the deflection (i.e. G_k has been increased from 4 kN/m² to 7.44 kN/m²). Infact, this load has not been increased, the total design axial compression for 1/5-scaled model would be 92.88 kN which is close to the scaling rule's result.

Fire compartment, which was considered externally fully glazed over 3.0 m height for the prototype, is also been scaled down. The properties of it are shown in Table 17.

Table 13. The section properties of small-scaled columns.

Section properties	Internal	Edge	Corner
Depth of section "h" (mm)	55.26	44.44	41.24
Width of section "b" (mm)	52.26	41.02	40.86
Thickness of web "s" (mm)	3.06	2.54	1.58
Thickness of flange "t" (mm)	5.06	4.10	2.50
Root radius "r" (mm)	2.54	2.04	2.04
Depth between fillets "d" (mm)	40.06	32.16	32.16
Ratios for local buckling of flange "$b/2t$"	5.16	5.00	8.17
Ratios for local buckling of web "d/s"	13.10	12.66	20.35
Second moment of area for axis x-x "I_x" (cm^4)	36.05	15.12	8.41
Second moment of area for axis y-y "I_y" (cm^4)	12.05	5.00	2.85
Elastic modulus of axis x-x "Z_x" (cm^3)	13.05	6.80	4.08
Elastic modulus of axis y-y "Z_y" (cm^3)	4.61	2.39	1.39
Plastic modulus of axis x-x "S_x" (cm^3)	14.95	7.82	4.54
Plastic modulus of axis y-y "S_y" (cm^3)	7.02	3.65	2.11
Area of section "A" (cm^2)	6.72	4.40	2.65

Table 14. General specification of columns.

General Specifications of Columns	
Characteristic of floor loading	$G_k = 7.44\ kN/m^2$ $Q_k = 5.0\ kN/m^2$
Floor and column sizes	Span B = 6 m Span L = 1.2 m Column height = 0.8 m
Material properties	Steel grade, $f_y = 275\ N/mm^2$ Elastic modulus, $E = 210000\ N/mm^2$

Table 15. Scaled properties of insulation for small-scaled columns.

Properties of Protection Material	Internal	Edge	Corner
Material	Box protection	Box protection	Box protection
Thickness, d_p	55.9 ≈ 55 mm	67 ≈ 70 mm	78 ≈ 80 mm
Density, ρ_p	1300 kg/m^3	1300 kg/m^3	1300 kg/m^3
Specific heat, c_p	1000 J/kg°K	1000 J/kg°K	1000 J/kg°K
Thermal conductivity, λ_p	0.50 W/m°K	0.50 W/m°K	0.50 W/m°K

Table 16. Design properties of small-scaled internal columns.

Design Specifications of Internal Columns	
Selected section	1/5-scaled of UC 254×254×132
Floor area	1.44 m²
Section classification	Web, d/s = 13.1 (Section is Class 1) Flange, $b/2t$ = 5.16 (Section is Class 1)
Ultimate limit state design at ambient temperature	Partial factor, γ_G = 1.35 and $\gamma_{Q,1}$ = 1.5 Design loads, G_d = 14.46 kN/m Q_d = 10.8 kN/m One floor total load = 25.26 kN Number of floors = 5 Design load from upper 4 floors = 101.04 kN Extra factored dead load (cladding, etc.) = 4.5 kN Total design axial compression load, N_{sd} = 130.8 kN
Design at room temperature	Buckling resistance, $N_{b,Rd}$ = 135.27 kN $N_{b,Rd} > N_{sd}$ (OK)
Buckling resistance at time t with uniform θ_a $(N_{bi,fi,t,Rd})$ and design load in fire $(N_{fi,sd})$	$(N_{bi,fi,t,Rd})$ = 123.95 kN $N_{bi,fi,t,Rd} > N_{fi,sd}$ =65.92 kN (OK)
Fire resistance time	t = 40.25 minutes $(t \sim s^{1/2})$

Table 17. Scaling of fire compartment.

Opening and Enclosure	
Floor area, A_f	1.44 m²
Total vertical opening, A_v	0.72 m²
Average of windows height on all walls, h_{eq}	0.6 m
Total area of enclosure, A_t	6.72 m²
Density of wall material, ρ_w $(\rho_w \sim s^{3/2})$	143.11 kg/m³
Specific heat, c_w $(c_w \sim s^{3/2})$	75.13 J/kg°K

Fig. 11 shows the protected and unprotected internal columns' temperature at small scale. For the small-scale model, there is no temperature change until almost 15 min due to the modelled insulation thickness. The protected steel temperature reaches around 512°C whereas unprotected temperature for the same internal column reaches to almost Standard fire temperature at the end of 90 minutes.

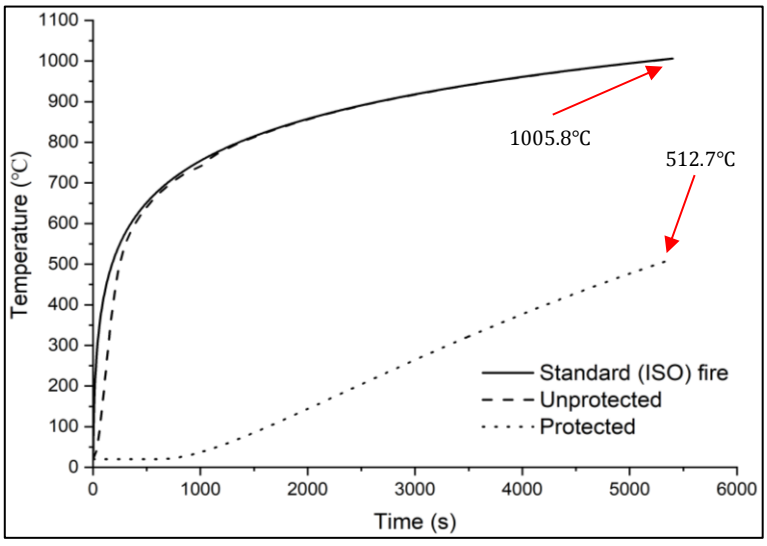

Fig. 11. Temperature distribution for internal columns at small scale.

5.2.2. Design of small-scaled edge columns

Except the axial compression load from 4 upper floors which is the half of the design loads of internal columns due to the design floor area, entire properties are identical with the small-scaled internal columns. The summary of modelling of edge columns is shown in Table 18.

This modelling results show that the differences between the buckling resistance at time t with uniform θ_a and the design load value increases for edge columns compared to the internal columns which results in reduce on the thickness of fire protection material. Hence; when the section size gets smaller, the differences between the buckling resistance of columns and design axial compression will be higher. The same fire compartment with its properties has been considered herein.

Fig. 12 presents the temperature distribution on small scaled edge columns. Because of scaling of insulation thickness, the lower protected temperature results have been obtained. The final temperature for the protected steel sample is around 320°C at the end of the 90 min. This means that there is almost no strength change of the steel material as the steel properties change dramatically after around 500°C.

Table 18. Design properties of small-scaled edge columns.

Design Specifications of Edge Columns	
Selected section	1/5-scaled of UC 254×254×86
Floor area	0.72 m²
Section classification	Web, d/s = 12.66 (Section is Class 1) Flange, $b/2t$ = 5.002 (Section is Class 1)
Ultimate limit state design at ambient temperature	Partial factor, γ_G = 1.35 and $\gamma_{Q,1}$ = 1.5 Design loads, G_d = 7.23 kN/m Q_d = 5.4 kN/m One floor total load = 12.63 kN Number of floors = 5 Design load from upper 4 floors = 50.52 kN Extra factored dead load (cladding, etc.) = 4.5 kN Total design axial compression load, N_{sd} = 67.65 kN
Design at room temperature	Buckling resistance, $N_{b,Rd}$ = 75.26 kN $N_{b,Rd} > N_{sd}$ (OK)
Buckling resistance at time t with uniform θ_a $(N_{bi,fi,t,Rd})$ and design load in fire $(N_{fi,sd})$	$(N_{bi,fi,t,Rd})$ = 112.56 kN $N_{bi,fi,t,Rd} > N_{fi,sd}$ =31.83 kN (OK)
Fire resistance time	t = 40.25 minutes $(t \sim s^{1/2})$

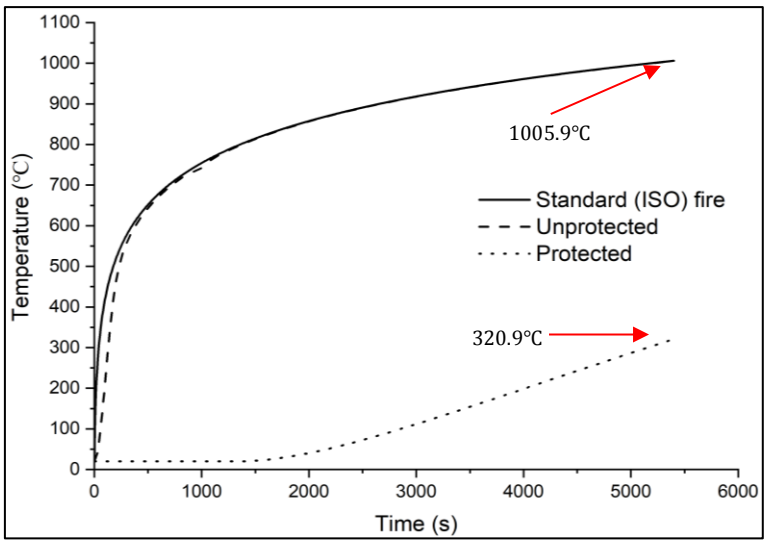

Fig. 12. Temperature distribution for edge columns at small scale.

5.2.3. Design of small-scaled corner columns

Small-scaled corner columns have been modelled with the same procedure of internal and edge columns. The properties are shown in Table 19.

Figs. 11-13 present the steel temperature on internal, edge and corner columns at small scale respectively. Although it has been mentioned in the Section 2.2as the changing the insulation property in terms of density and thermal conductivity is impracticable and unpredictable because of non-exist of light-weight insulation materials in the design procedure, using the same insulation thermal properties with the full-scale produced very lower temperatures since the insulation thicknesses are scaled according to the "$s^{-1/2}$" (Wang, 2006) resulting in thicker insulation material for the reduced scale models. Therefore, an important outcome from the study is to scale the insulation thermal properties.

Table 19. Design properties of small-scaled corner columns.

Design Specifications of Corner Columns	
Selected section	1/5-scaled of UC 254×254×52
Floor area	0.36 m^2
Section classification	Web, d/s = 20.35 (Section is Class 1) Flange, $b/2t$ = 8.17 (Section is Class 1)
Ultimate limit state design at ambient temperature	Partial factor, γ_G = 1.35 and $\gamma_{Q,1}$ = 1.5 Design loads, G_d = 3.62 kN/m Q_d = 2.7 kN/m One floor total load = 6.32 kN Number of floors = 5 Design load from upper 4 floors = 25.28 kN Extra factored dead load (cladding, etc.) = 4.5 kN Total design axial compression load, N_{sd} = 36.1kN
Design at room temperature	Buckling resistance, $N_{b,Rd}$ = 80.8 kN $N_{b,Rd} > N_{sd}$ (OK)
Buckling resistance at time t with uniform θ_a $(N_{bi,fi,t,Rd})$ and design load in fire $(N_{fi,sd})$	$(N_{bi,fi,t,Rd})$ = 70.71 kN $N_{bi,fi,t,Rd} > N_{fi,sd}$ =15.92 kN (OK)
Fire resistance time	t = 40.25 minutes $(t \sim s^{1/2})$

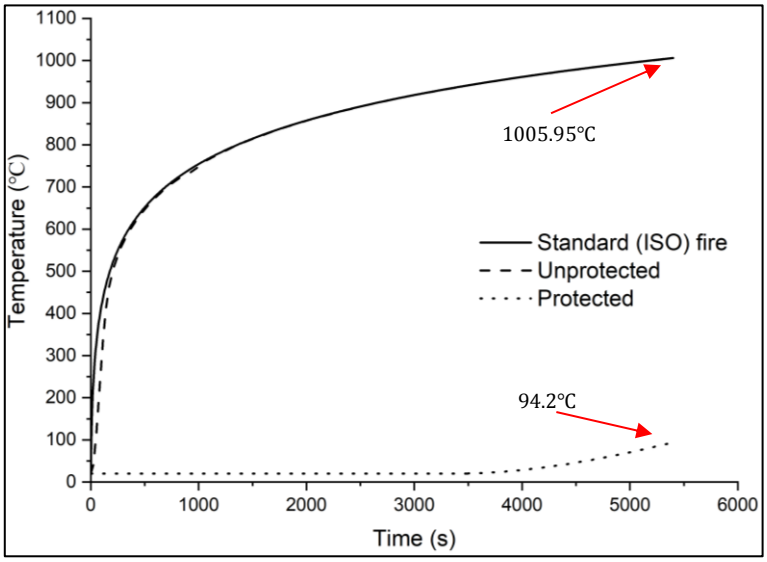

Fig. 13. Temperature distribution for corner columns at small scale.

6. Conclusions

The feasibility of using small-scale models to investigate the fire performance of composite structures has been explored in this paper. The physical scaling rules for the composite structures in general and insulation have been presented. Reduced scale model testing is a significantly economical way compared with the full-scale tests. Providing proper and correct scaling conditions, these small-scale models can represent the behaviour of real structures under a fire condition. The modelling results in terms of beam, slab and column according to the presented scaling rules have been predicted by using developed Fire Excel Spreadsheets and MATLAB. The following inferences can be made from this study:

- The scaling factor ($s = 1/5 - \text{scale}$) geometrically has been applied to all structural members, fire compartment and insulation. The section sizes and the insulation thicknesses has been modelled according to scaling rules.
- The insulation thermal properties including density and thermal conductivity should also be scaled rather than considering it as light-weight material with ignoring the scaling. This results in very lower temperatures for the small-scaled steel samples.
- The comparisons of results between different types of columns, and effective and appropriate strategy for partial scaling have been presented.
- The required protection material in the reduced scale model, box protection herein this study, is more than that required in the real structure to resist the structure to the proposed fire resistance time.
- The loads used in the real structure have been increased by including additional sand bags to ensure the same deflection in prototype.
- Temperature results of steel profiles in the model are close to the temperatures of real structure. This makes the small-scale modelling methodology an economical way to guess the behaviour of real structures under fire condition.
- The comparison of critical temperatures of beams between small-scale and full-scale is quite good and promising. The relative difference is within 6%. This leads to that failure mechanism, failure time (fire resistance time for unprotected sections) and failure temperature can represent the prototype.
- A small-scale composite slab is designed with micro concrete and black annealed wire. However, the fabrication of wires is a complex process since they are so thin. Therefore, they need to be produced carefully to represent the similar behaviour with the full-scaled composite slab.

The scaling rules are applied to open sections herein this study. However, those mentioned rules can also be easily applied on the closed sections such as rectangular hollow sections (RHSs).

REFERENCES

Bjørge J, Metallinou MM, Kraaijeveld A, Log T (2017). Small scale hydrocarbon fire test concept. *Technologies,* 5(4), 72.

CEN (2005a). EN 1993-1-2: Eurocode 3. Design of Steel Structures. *Part 1.2: General Rules - Structural fire design.* BSI, London.

CEN (2005b). EN 1994-1-2:2005: Eurocode 4. Design of Composite Steel and Concrete Structures – Part 1-2: General Rules – Structural Fire Design. *Part 1-2: General Rules – Structural Fire Design.* BSI, London.

Chattaway A, Cox GG, Preece SR, Spring DJ (1997). The development of a small scale class a fire test. *Halon Options Technical Working Conference (HOTWC).* Albuquerque, New Mexico.

Cutter PA, Shenoi RA, Phillips HJ, Moy SSJ (2009). A new small scale fire resistance test method for composite materials. *ICCM International Conferences on Composite Materials.* Edinburgh, UK.

Girardin B, Fontaine G, Duquesne S, Bourbigot S (2016). Fire tests at reduced scale as powerful tool to fasten the development of flame-retarded material: Application to cables. *Journal of Fire Sciences,* 34(3), 240-264.

Harris HG, Sabnis G (1999). *Structural Modeling and Experimental Techniques* (2nd ed.). CRC Press, Florida.

International C (2007). ComFlor Decking System Composite Floor Decks. Corus Group.

ISO (2014). Fire-resistance tests - Elements of building construction - ISO 834-11. I. O. f. S., Geneva, Switzerland.

Krajčír M, Müllerová J (2017a). 3D small-scale fire modeling experiments. *Procedia Engineering,* 192, 474-479.

Krajčír M, Müllerová J (2017b). 3D small-scale fire modeling testing preparation. *Procedia Engineering,* 192, 480-485.

Lannon CM, Stoliarov SI, Lord JM, Leventon IT (2018). A methodology for predicting and comparing the full-scale fire performance of similar materials based on small-scale testing. *Fire and Materials,* 42(7), 710-724.

Müllerová J (2016). Flashover Fire Modelling by Real Small-Scale Models. *In:* International Multidisciplinary Scientific GeoConference: SGEM: Surveying Geology & Mining Ecology Management, Sofia, 305-310.

O'connor DJ, Morris B, Silcock GWH (1997). A Model Fire Test for Parametric Testing of Half Scale Structural Components. *In:* Fire Safety Science 5. International Association for Fire Safety Science, 997-1008.

O'Connor DJ, Silcock GWH (1992). A strategy for the fire testing of reduced scale structural models. *Fire Technology,* 28(1), 48-69.

Quintiere JG, Carey AC, Reeves L, McCarthy LK (2017). Scale Modeling in Fire Reconstruction. US.

Quintiere JG, Su GY, Schultz N (2007). Physical Scaling for water mist fire supression - a design application. *International Journal on Engineering Performance-Based Fire Codes,* 9(2), 87-108.

Radzi NAM, Hamid R, Mutalib AA (2016). A review of methods, issues and challenges of small-scale fire testing of tunnel lining concrete. *Journal of Applied Sciences,* 16(7), 293-301.

Wang M (2006). Scale Modeling of Structural Behavior in Fire. *Ph.D. thesis*, University of Maryland.

Wang M, Chang P, Quintiere J, Marshall A (2007). Scale modeling of the 96th floor of world trade center tower 1. *Journal of Performance of Constructed Facilities,* 21(6), 414-421.

Wang M, Perricone J, Chang PC, Quintiere JG (2008). Scale modeling of compartment fires for structural fire testing. *Journal of Fire Protection Engineering,* 18(3), 223-240.

Wijayasri S (1983). Modelling of Concrete Structures. *Ph.D. thesis*, University of East London.

Wilson DP (2018). Numerical Simulations of Small-scale and Full-scale Fire Experiments. *M.Sc. thesis*, University of Waterloo.

Challenge Journal of Concrete Research Letters

Research Article

Diffusion study of chloride and binding of water in concrete pore by molecular dynamics simulation using LAMMPS

Md. Shafiqul Islam [a], Sayem Ahmeed [a,*], Sumon Kumar Ghosh [a]

[a] *Department of Civil Engineering, Rajshahi University of Engineering & Technology, Kazla 6204, Rajshahi, Bangladesh*

ABSTRACT

As for the communication between concrete and the particles, the surface shows Cl– shock and Na adsorption. With expanded particle focus, the solid adsorption capacity for Cl– is upgraded as a result of a detailed overview of the dynamic molecular simulation studies examining the chloride diffusion coefficient. Different characteristics of the diffusion process, including molecular models, system-size effects, temperature, and pressure conditions, and the type of protection, are discussed. This paper focus on Molecular Dynamic Simulation to determine the diffusion coefficient of chloride ion and water molecules in concrete. The diffusion coefficient for NaCl salt obtained $6.60178x10^{-10}m^2/s$ and the diffusion coefficient for $CaCl_2$ salt obtained $7.29305x10^{-10}m^2/s$. So, the average chloride diffusion coefficient $6.9475x10^{-10}m^2/s$. Diffusion coefficient obtained from graph $5.562x10^{-10}m^2/s$. Diffusion coefficients for water molecules for NaCl solution are $6.125x10^{-10}m^2/s$, $6.85x10^{-10}m^2/s$, $1.044x10^{-10}m^2/s$, $8.525x10^{-10}m^2/s$, $6.25x10^{-10}m^2/s$. diffusion coefficient of water molecules in $CaCl_2$ solution are $4.5x10^{-10}m^2/s$, $6.725x10^{-10}m^2/s$, $1.254x10^{-10}m^2/s$, $7.725x10^{-10}m^2/s$, $1.3x10^{-10}m^2/s$. Average value obtained for water molecule diffusion are $4.545x10^{-10}m^2/s$, $7.4062x10^{-10}m^2/s$ and $1.149x10^{-10}m^2/s$. This diffusion of chloride effects the binding of water in concrete pore.

ARTICLE INFO

Article history:
Received 17 February 2021
Revised 29 April 2021
Accepted 4 August 2021

Keywords:
Diffusion coefficient
Molecular dynamic simulation
Concrete
Chloride ion

1. Introduction

Cement is the most consumed substance on construction purpose. On average three tons of concrete are consumed annually by every human being living on Earth. Cement is one of the most widely accepted materials in the world. Concrete is the second most. The cement industry accounts for almost 5-7% of global carbon dioxide (CO2) emissions. Despite its other pollution, the industry is the third-largest producer of greenhouse gasses in the world. Besides, cement production is the third-largest energy consumer sector. On the other hand, in hostile conditions such as seawater, the Cl^- ions may enter the cement paste and contribute to the deterioration of the reinforcement (Arya and Xu, 1995; Page et al., 1986). It has a harmful effect on the durability of the structure.

Diffusion is a very important parameter such that sometimes specification is presented with regards to diffusion (Honorio et al., 2019). As Chloride diffusion water diffusion is also an important parameter. It has an inverse relationship with strength of concrete. High strength concrete has a lower diffusion coefficient, where low strength concrete has a higher diffusion coefficient (Balakrishna et al., 2018). Moreover interaction between water and C-S-H gel may have a substantial effect on the cohesion force (Bonnaud et al., 2012; Lesko et al., 2001).

To interpret the diffusion process in various length scales, it is important to explore the origin of the property at the molecular level. Calcium silicate hydrate(C-S-H) is the fundamental hydration result of concrete powder and water. Concrete hydrates have a multi-scale permeable structure that contains capillary pores and gel pores (Ma and Li, 2013). Transport of the water in the permeable medium has an incredible impact on the strength, creep, shrinkage, and compound and actual

* *Corresponding author*. Tel.: +880-19-0916-3495 ; E-mail address: sayemahameedruet15@gmail.com (S. Ahmeed)
ISSN: 2548-0928 / DOI: https://doi.org/10.20528/cjcrl.2021.03.002

reactivity of concrete glue. From one viewpoint, ecological changes, for example, the temperature, moistness, and stacking, can bring about water content varieties in C-S-H gel. Then again, in an aggressive environment, for example, ocean water, the Cl– particles can infiltrate the concrete glue and lead to the erosion of reinforcement (Arya and Xu, 1995; Page et al., 1986). It detrimentally affects the solidness of the structure.

To decipher the dissemination system at various length scales, it is important to explore the inception of the property at a sub-atomic level. The 1H NMR test explored the properties of water in the nano-pores of C-S-H gels (Wang et al., 1998) and the quasi-elastic neutron scattering (QENS) method (Bordallo et al., 2006).

The physical and structural properties of water can vary substantially between bulk water and near surface water as surfaces tends to disturb fluid structure up to a certain atomic diameter from surface. This phenomena can be used to understand the chemical properties of mineral pore surface. However even after various studies and methods have been carried out to find the difference, it's still not completely understood. Here molecular dynamics can help to accelerate the advancement of understanding (kalinichev et al., 2007). Although previous researchers had obtained various creative methods molecular dynamics can be more helpful in understanding what happens at atomic level. It is a well suited tool to understand specific ion effects in aqueous solution. It was also has been extensively used in past to understand this phenomena (Honorio et al., 2019).

In this study tobermorite 11A is used as cement molecule as it has similarities with C-S-H which is the building block of cement paste. As the modeling of micropore is both time consuming and not practical for computer based atomistic simulation. Modelling micropore can solve this problem as well as give accurate result. So a pore size of 60A is chosen which was a gel pore and can give very accurate result.

2. Method and Methodology

2.1. Simulation model

Methods for crystal analogues are commonly used to model C-S-H gel. In this analysis, Hamid's 11Å tobermorite structure (Hamid 1981) is considered. A few modifications, such as adding calcium ions and hydroxyl groups to the tobermorite structure, must be done to have a crystal stone structure equal to the actual structure of C-S-H gel (Kurczyk and Schwiete, 1962), Inclusion of tobermorite between portlandite sheets (Kantro et al., 1962), integration into the portlandite system of silicate monomer groups (Shpynova et al., 1967), consideration of some calcium ions and hydroxyl groups in the structure and interlayer spaces between tobermorite silicate chains (Taylor and Howison, 1956) the elimination of such bridging tetrahedral silicon groups and the insertion of interlaminar calcium ions (Garboczi and Bentz, 1992). No improvement in the replication model has been considered in this paper and particular forms of previously described crystal are studied. For the evaluation of complex properties such as surface interactions and transportation characteristics, it is entirely required to reveal substrates at the recreation finishes enclosing and a nanopore the supercell core that combines the anion and cation fluid structure. Previous experts for tobermorite have revised this technique (Kalinichev and Kirkpatrick, 2002; Buenfeld et al., 2014) and other hydrates such as portlandite, Friedel's salt, AFM phases, Aft phases, brucite, and gibbsite (Yu and Kirpatrick, 2005; Kalinichev et al., 2007).

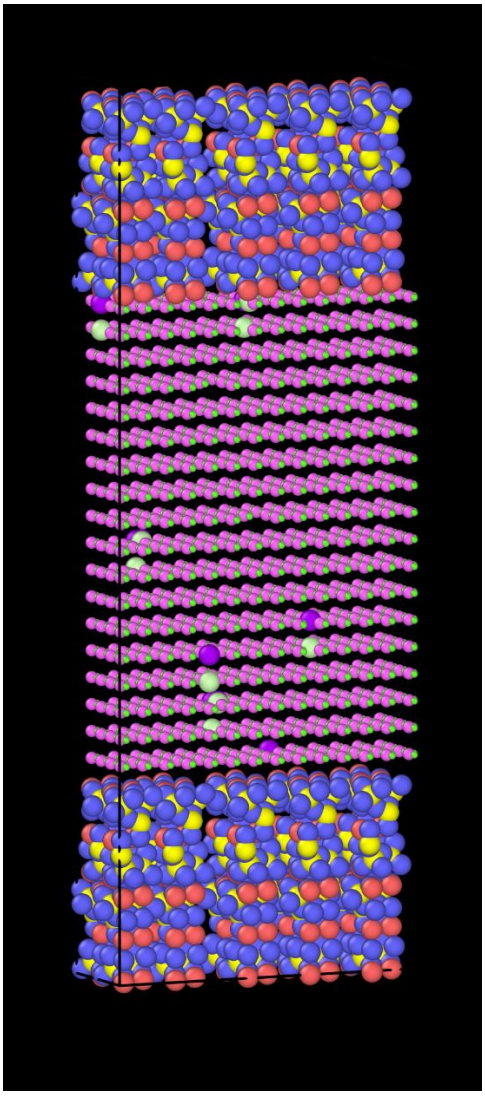

Fig. 1. Snapshot of the simulation cell captured by OVITO (purple represents Oxygen atoms, green represents Hydrogen, light green represents Chloride ions, violet represents Sodium, red represents Calcium, Blue represents Silicon).

2.2. Simulation settings

Molecular dynamics (MD) is usually used at the atomistic level to provide a superior understanding of matter and individual interactions between particles or atoms and to determine specific material properties (Gopalakrishnan et al., 2011). MD is ideal for measuring time-subordinate properties, such as the coefficient of diffusion.

The Molecular Dynamics simulation methodology was performed using LAMMPS in this analysis. The diffusion coefficient of chloride ions is variable for various pore sizes. For this simulation cell model, the temperature was 273°C (300°K). For the simulation the NVT ensemble was used, which was a canonical ensemble, where the number of particles which is represented by N, the volume of the system which is represented by V, and the temperature of the system which is represented by T were conserved and rest of the variables were allowed to vary to compensate the changes that were applied to the model. To run the model, the initial relaxation time was 500ps, as the simulation was run for 2200 ps. The thermostat that conserved the energy was both exothermic and endothermic. For the analysis of the input file that was provided to LAMMPS time step was set to 1fs enabling calculation to be sufficiently accurate. The dump file was generated by extracting the atomic positions and velocities for every 100time steps or 100 fs, enabling the dump file to contain 220,000 different atomic positions and velocities which was used to visualize in a MD visualization software called OVITO, and later for calculating the required data. Here the results were statistically reliable as the simulation was run for 2200ps or 2.2ns, which is well above 0.5 ns. On top of that the number of atoms were large enough and the super-cell size was big enough to provide further reliability (Buenfeld et al., 2014).

It is important depending on the point of interest of MD simulation. Diffusion coefficient, the force field and potential as well as the atomic positions. The same can be said for the case salt properties on LJ potential parameters such as σ and ε (Table 1). Running the model using a MD software certain values of these σ and ε will give the most accurate results such as solubility, alkalinity and acidity of the salt water solution. Same can be assumed for the water molecule. The molecular trajectory of the water, the motion of the water in the super-cell, the transportation capacity of water etc. will depend heavily upon these potential parameters.

In this study the Sodium Chloride (NaCl) and the water molecule were ensured to be stable in their crystal structure.

This parameter shown in the above table are used for the simulation. Here, 1Å is 100 Pico meter and *e* is the charge of single electron or proton which is 1.602x10-19 C.

Table 1. Lennard Jones potentials.

Model	ε (kJ/mol)	Σ (Å)	q (e)	m (g/mol)
Na	0.600	2.440	+1	22.9897
Ca	0.540	3.270	+1	40.0780
Cl	0.054	4.830	-1	35.4530
H	0.000	0.000	+0.4236	1.00794
O	0.650	3.166	-0.84720	15.9940

3. Data Analysis and Calculations

To find the diffusion coefficient of the model, a kinetic study was used. It is useful to find that there are three procedures of determination of the diffusion coefficient. The first way to find the coefficient is by using the velocities of the ions (or molecules). In this method, the diffusion coefficient can be obtained by the integration of the Velocity Autocorrelation Functions (VAF). A good example of this is the Green Kubo relations (Haile 1992). The second method is Force Autocorrelation which is used to calculate the diffusion over the energy barrier and uses the fluctuation-dissipation system. In this case, the molecules are set where it is desired and the force that is acting on them in time, $F(t)$ is taken. In this method the diffusivity is nothing but the correlation of time. The last method uses the positions of the molecules and by the information the Mean Squared Displacement or MSD is obtained to get the diffusion coefficient. The end result given by each method is more or less the same and any one of them can be used depending on what the end goal is. In this study, LAMMPS is used to calculate the diffusion coefficient using the third method or MSD.

3.1. Diffusion coefficient from MSD (NaCl)

The diffusion of the water was studied first. For this The Mean Square Displacement (MSD) values were obtained from LAMMPS. Upon starting the initial positions $r_i(0)$ were set to all particles by using the MSD. Then the displacement for each particle was calculated with respect to their positions. Here Einstein diffusion coefficient formula can be applied, which can be expressed as follows r_i.

$$MSD = \frac{1}{N}\sum_{i=1}^{N}(\overrightarrow{r_i}(t) - \overrightarrow{r_i}(t_0))^2 \quad (1)$$

$$D = \lim_{t\to\infty}\left(\frac{\langle(r(t)-r(0))^2\rangle}{n}\right)^n \quad (2)$$

where r_i is the location of a particle at step I, and N is the number of frames dumped from the *MD*. The diffusion coefficient is D, t_0 is the initial time of simulation and d is the dimensionality of the system.

Fig. 2 is a graph of *MSD* values that were obtained from LAMMPS for Chloride ions for Sodium Chloride solution. It should be noted that the values are only after the simulation had been run, so the initial relaxation time is not present in the graph.

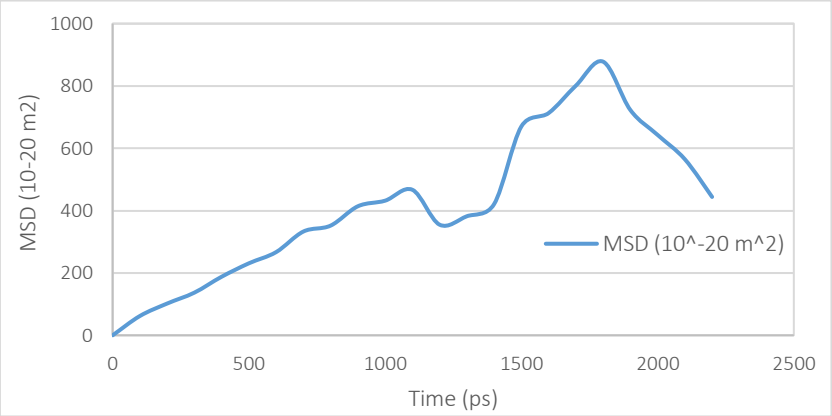

Fig. 2. MSD vs. time graph for Chloride ions in NaCl solutions.

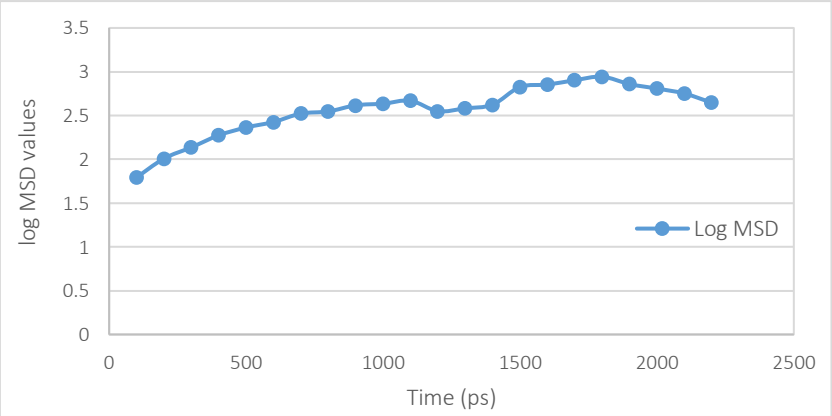

Fig. 3. Log MSD vs. time graph for Chloride ions in NaCl solutions.

In Einstein's formula, the dimensionality d is taken as 3 for three dimensional systems. For d=3 the formula can be simplified as:

$$MSD = 6Dt \quad \text{or} \quad D = \frac{MSD}{6t} \tag{3}$$

Here D, MSD and t are all in SI units. The unit style that is used in LAMMPS is real, which means MSD is in Å^2, D is in Å^2/s, and time is in picoseconds. So, they were converted in SI units by 1Å = 10^{-10} m, 1ps = 10^{-12} seconds.

3.2. Diffusion coefficient from MSD ($CaCl_2$)

As mentioned earlier for Sodium Chloride and Calcium Chloride simulation models were built separately and calculated separately. The calculation of the diffusion coefficient for Chloride ions in Calcium Chloride solution is carried out in the same way. First, the MSD values were extracted from the LAMMPS simulation and the values were put in a graph (Fig. 4).

After that, the log values of the Cl ions were put into the graph in the same way (Fig. 5).

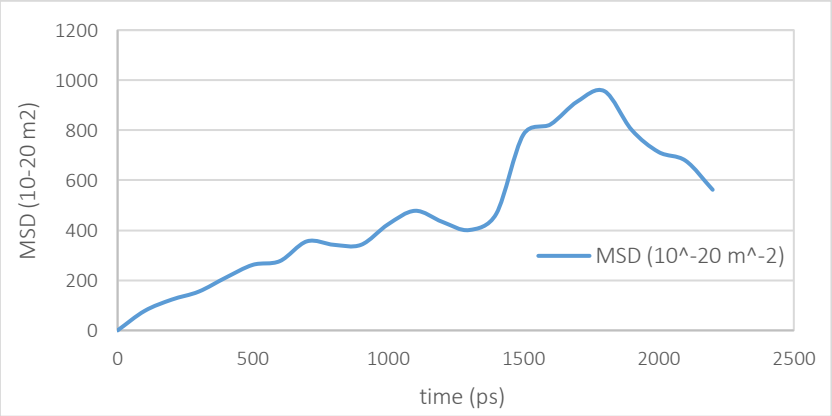

Fig. 4. MSD vs. time graph for Chloride ions in $CaCl_2$ solutions.

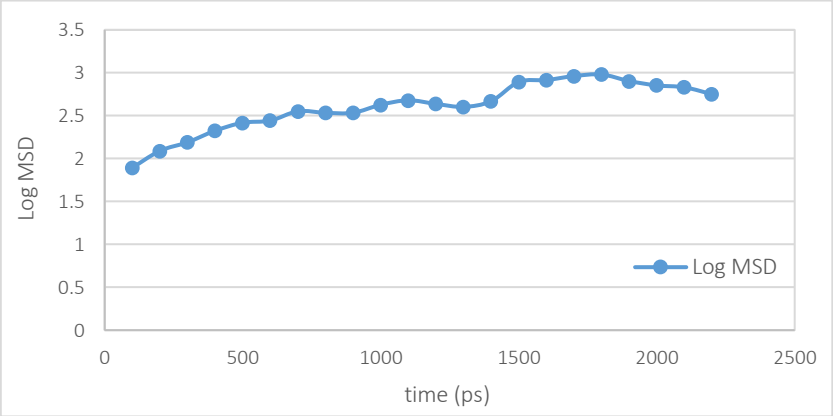

Fig. 5. Log MSD vs. time graph for Chloride ions in $CaCl_2$ solutions.

Using Einstein's formula, the diffusion coefficient of the Chloride ions in Calcium Chloride is calculated.

3.3. Diffusion coefficient of water molecule

The 992 water molecules were divided into two major groups. They are the intermolecular water molecules and the intra moleculer water molecules. Their MSD values and diffusion coefficient were calculated using LAMMPS and Einstein's formula respectively. First, the MSD values from LAMMPS were plotted in a graph which was also done for the Chloride ions (Fig. 6).

To calculate the diffusion coefficient of water the MSD values obtained from LAMMPS were used. But before that from the position of each atom, the density of the water molecule was calculated. The position of the water molecule is contained in the dump file that was created after simulating LAMMPS.

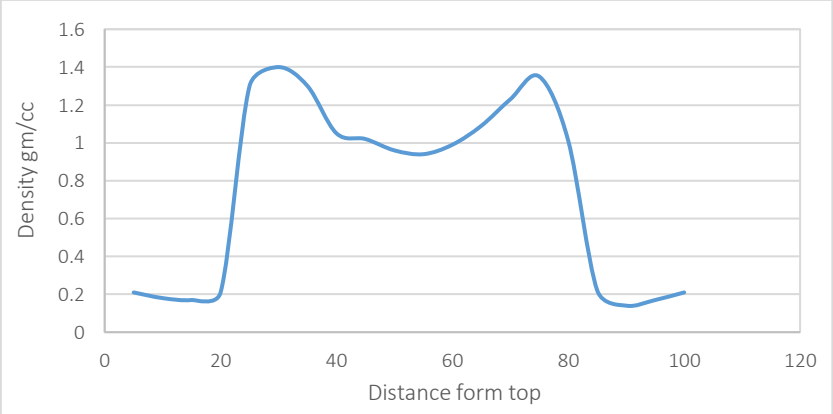

Fig. 6. Density of water vs. distance from top in *z*-axis.

As mentioned earlier the total dimension in the *z*-direction is 100Å. The top and bottom 20 Å is occupied by tobermorite atoms. Rest of the 60 Å is the pore space in the simulation model, which contains NaCl or $CaCl_2$ solution. From counting the number of each atom in a small local region the density of the water at that particular region can be obtained. The values were automatically obtained from LAMMPS.

The top part of the graph shows the water molecules were densely concentrated near the substrates. It shows that the middle part had a density of water of about 1 gm/cc. It indicates that for the middle one third the value of the density did not change from its initial value. If we look closely at Fig. 6, we can notice that the values of distribution mirror from the middle centreline of the nanopore, which makes it symmetrical along the middle of the pore. After calculating the diffusion coefficient values from MSD that were provided by LAMMPS.

4. Result and Discussion

4.1. Diffusion coefficient of chloride ions

From Eq. (3) the values of diffusion coefficient were calculated from MSD values. The results thus obtained for Chloride molecules for different time steps. The values were averaged to get the diffusion coefficient of the Chloride ions for both salts. The value of diffusion coefficient obtained for NaCl salt solution is 6.60178×10^{-10} m^2/s and for $CaCl_2$ solution is 7.29305×10^{-10} m^2/s. And the diffusion coefficient obtained by averaging these two values is 6.9475×10^{-10} m^2/s. The diffusion coefficient values obtained by previous researchers are 1.07×10^{-9} m^2/s for cement paste (experimental) (Pivonka et al., 2004) and 7.097×10^{-10} for Hamid's 11Å tobermorite (Behnam and Amir, 2017). The values obtained in this study is thus satisfactory with previous researchers.

Figs. 7 and 8 show the comparison of MSD values for NaCl and $CaCl_2$ solutions. From the figures we can see that the MSD values are almost close for both salts. So, their diffusion coefficient should also be similar, which is true for the values obtained in this study. The values are only 5% apart for two types of salt. Hence, it can be said that the diffusion coefficient of Chloride ion does not matter too much on the type of salt.

This diffusion coefficient is obtained from the MSD values by using Einstein's formula. It can also be calculated form the slope of the log MSD graph. The slope of the log-MSD graph is shown in Fig. 8. From the slope the obtained diffusion coefficient is 5.562×10^{-10} m²/s. This is almost similar to the value obtained by using Einstein's formula.

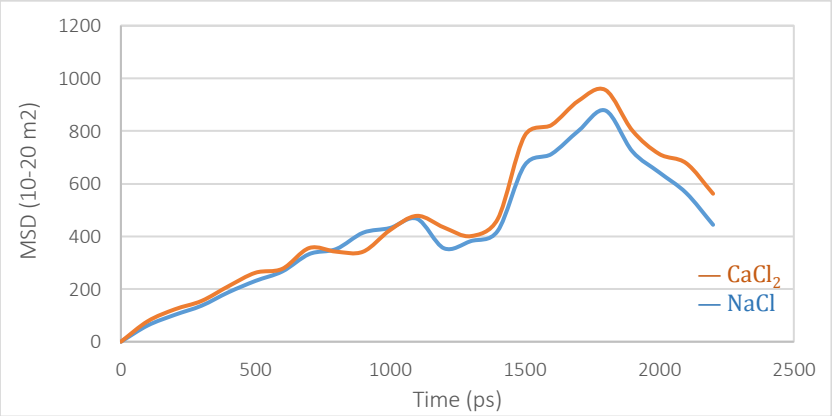

Fig. 7. MSD vs time graph for Chloride ions in NaCl and $CaCl_2$ solutions.

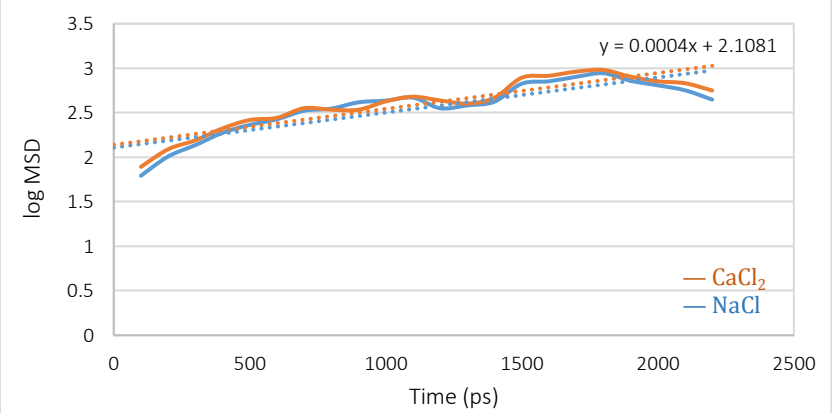

Fig. 8. Log MSD vs. time graph for Chloride ions in NaCl and $CaCl_2$ solutions.

4.2. Diffusion coefficient of water molecule

The water molecules in the simulation model can be divided into three categories. The first is Intra-molecular water molecules, which is in the tobermorite layer. Such water molecules are entrapped by the tobermorite molecules and have very little freedom to move. The second category is the water molecules near the surface of the tobermorite layer. This represents the inner surface of a concrete nano-pore. Here, the water molecules are subjected to the adsorption by the electrostatic interaction with tobermorite molecules. So, there movement is supposed to be restricted by a bit. The third category is the water molecules which are situated in the within the region equal to the height of one third of the pore space from either side of the centreline. Here, the water molecules should behave just like the free water molecules because the distance from the tobermorite layer is too high to be affected by the adsorption. To be free from the adsorption the distance of the water molecule should be least 3 times the radius of the water molecule, which is roughly 8-10Å (Kalinichev et al., 2007), which is true for this category.

In Figs. 9 and 10, the variation of diffusion coefficient values and their initial positions in the primary configuration is shown. The diffusion coefficient of intra-layer water s are at the beginning and end part of the graph in Figs. 9 and 10. The curve line is gotten by the average value of the diffusion coefficient for specific locations. Water molecules can be grouped into two types. They are the interlayer and intralayer. The interlayer molecules can be further divided into two groups. They are molecules near the pore surface and molecules near the middle 1/3rd of the pore.

For the Intra-space of NaCl solutions diffusion coefficient of water molecules at top is 6.125×10^{-11} m²/s and for molecules of waters at bottom is 6.25×10^{-11} m²/s. And for $CaCl_2$ solution this value is 4.5×10^{-11} m²/s for top

layer and 1.3x10^{-11} m^2/s for bottom layer. Average diffusion coefficient is 7.4685x10^{-11} m^2/s, which is close to previous researches. The previous researches show that the intralayer diffusion coefficient are 5.0x10^{-11} m^2/s (Kalinichev et al., 2007) and 1.4x10^{-11} m^2/s (Yoon and Monterio, 2013). The diffusion coefficient is relatively small in the intralayer spaces, mainly due to the water molecules that are present in here is a bit like crystal. They behave mostly like solid particles and are in a harmonic motion due to the force that was acted upon them, as they were trapped between the silicate chains as well as having a very powerful Hydrogen bond.

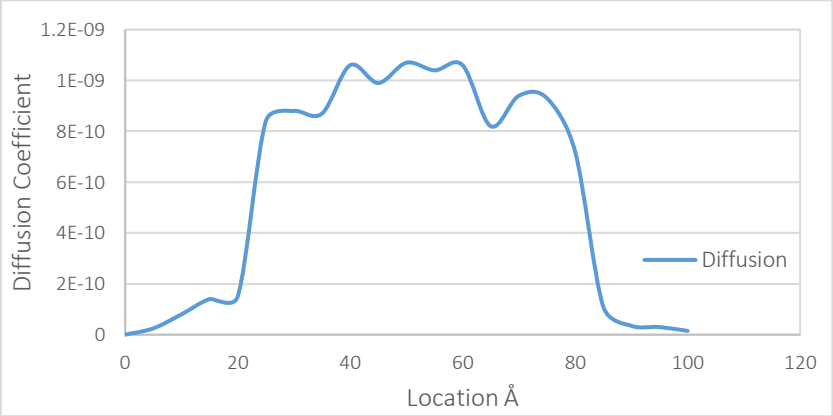

Fig. 9. Diffusion coefficient of water molecules in NaCl solution with respect to distance from the top.

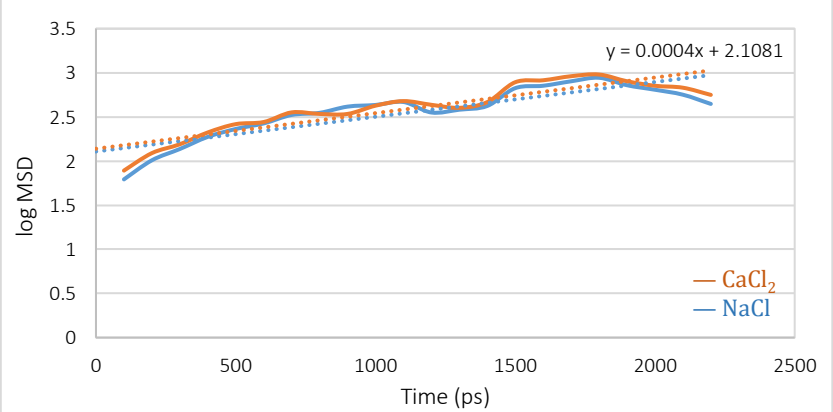

Fig. 10. Log MSD vs time graph for Chloride ions in NaCl and $CaCl_2$ solutions.

The interlayer part that is composed of two groups-near surfaces and near middle one third region.

For near surface water molecules in NaCl solution the diffusion coefficient at top is 6.85x10^{-10} m^2/s and 8.525x10^{-11} m^2/s at bottom. For $CaCl_2$ solution these values are 6.725x10^{-10} m^2/s at top and 7.725x10^{-10} m^2/s at bottom. The average value is 7.4685x10^{-11} m^2/s. The values obtained by previous researchers are 5x10^{-11} m^2/s (Kalinichev et al., 2007) and 1.4x10^{-10} m^2/s (Yoon and Monterio, 2013). This shows the obtained value in this study is close with previous researches.

For the molecules near the middle 1/3rd of the model is about 1.14x10^{-10}m^2/s to 1.23x10^{-10} m^2/s in NaCl and $CaCl_2$ respectively. The values obtained by the previous researches for free water molecules are 4.13x10^{-10}m^2/s by the SPC model (Buenfeld et al., 2014). The values indicate that the middle 1/3rd water molecules are less affected by the tobermorite surfaces. This phenomenon enables them to diffuse more freely and their distance is larger compared to other water molecules and close to the free water molecule.

5. Conclusions

Cement is the most consumed substance for construction purposes. On average three tons of concrete are consumed

Following conclusions were made from the results and observation of the study:

- The diffusion coefficient of Chloride ion is hardly affected by the type of salt. It is shown that the result obtained for one type of Chloride solution can be easily matched by other type of Chloride solution. This study shows only 5% difference between two types of salt. So, effect of Chloride ion ingress will cause equal effect for a cement paste, regardless of the salt. This statement is also supported by previous researchers, as the values matches with their.
- Surface binding of the water molecules have a bigger effect on the transportation of the water molecules in the cement nano-pore. The study shows that near surface water molecule has diffusion coefficient less than the molecules near middle by a factor of 36%.

REFERENCES

Arya C, Xu Y, Page (1995). Effect of cement type on chloride binding and corrosion of steel in concrete. *Cement Concrete Research,* 25(4), 893-902.

Balakrishna MN, Mohamad F, Evans R, Rahman MM (2018). Determination of water diffusion coefficient in concrete cubes for infinite time duration. *Science & Technology*, 4, 137-145.

Behnam Z, Amir T (2017). Diffusion study for chloride ions and water molecules in C-S-H gel in nano-scale using molecular dynamics: Case study of tobermorite. *Advances in Concrete Construction*, 4, 305-317.

Bonnaud PA, Ji Q, Coasne B, Pellenq RJM, Van Vliet KJ (2012). Thermodynamics of water confined in porous calcium-silicatehydrates. *Langmuir,* 28(31), 11422–11432.

Bordallo (2006). Water dynamics in hardened ordinary portland cement paste or concrete: From quasielastic neutron scattering. *The Journal of Physical Chemistry B*, 110(36), 17966-17976.

Buenfeld R, Glass GK, Hassanein AM, Zhang JZ (2014). Chloride transport in concrete subjected to electric field. *Journal of Materials in Civil Engineering,* 10(4), 220-228.

Garboczi EJ, Bentz DP (1992). Computer simulation of the diffusivity of cement-based materials. *Journal of Materials Science,* 27(8), 2083-2092.

Gopalakrishnan K, Birgisson B, Taylor P, Attoh-Okine NO (2011). Nanotechnology in Civil Infrastructure. Springer.

Haile JM (1992). Molecular Dynamics Simulation: Elementary Methods. Wiley, England.

Honorio T, Benboudjema F, Bore T, Ferhat M, Vourc'hc E (2019). The pore solution of cement-based materials: structure and dynamics of water and ions from molecular simulations. *Physical Chemistry Chemical Physics*, 21, 11111-11121.

Kalinichev AG, Kirkpatrick RJ (2002). Molecular dynamics modeling of chloride binding to the surfaces of calcium hydroxide, hydrated calcium aluminate, and calcium silicate phases. *Chemistry of Materials*, 14, 3539-3549.

Kantro DL, Brunauer S, Weise CH (1962), Development of surface in the hydration of calciumsilicates. II. Extension of investigations to earlier and later stages of hydration. *The Journal of Physical Chemistry,* 66(10), 1804-1809.

Kurczyk H, Schwiete H (1960). Concerning the hydration products of C3S and β-C2S, *Proceedings of the 4th International Symposium on the Chemistry of Cement*, 1, 349-358.

Lesko S (2001). Investigation by atomic force microscopy of forces at the origin of cement cohesion. *Ultramicroscopy*, 82(1-2), 11-21

Ma H, Li Z (2013). Realistic pore structure of Portland cement paste: Experimental study and numerical simulation. *Computers and Concrete,* 11(4), 317–336.

Pivonka P, Hellmich C, Smith D (2004), Microscopic effects on chloride diffusivity of cement pastes-a scale-transition analysis. *Cement Concrete Research,* 34(12), 2251-2260.

Shpynova L, Id N, Belov N (1967). Microstructure of alite cement stone (hydrated tricalcium silicate). *Soviet Physics Crystallography*, 11(6), 747.

Taylor H, Howison J (1956). Relationships between calcium silicates and clay minerals. *Clay Minerals Bulletin*, 3(16), 98-111.

Wang, Ferguson MM, Eng G, Bentz DP, Ferraris CF, Clifton JR (1998). 1H nuclear magnetic resonance characterization of portland cement: Molecular diffusion of water studied by spin relaxation and relaxation time-weighted imaging. *Journal of Materials Science*, 33(12), 3065–3071.

Yoon S, Monteiro PJ (2013). Molecular dynamics study of water molecules in interlayer of 14 å tobermorite. *Advanced Concrete Technology*, 11(6), 180-188.

Yu P, Kirkpatrick RJ (2005). 35Cl NMR relaxation study of cement hydrate suspensions. *Cement and Concrete Research,* 31(10), 1479-1485.

Challenge Journal of Concrete Research Letters

Research Article

Mechanical strength variation of zeolite-fly ash geopolymer mortars with different activator concentrations

Roble Ibrahim Liban [a], Ülkü Sultan Keskin [a], Oğuzhan Öztürk [a,*]

[a] *Department of Civil Engineering, Konya Technical University, 42250 Konya, Turkey*

ABSTRACT

Zeolite is of a significance for geopolymers as it is a natural precursor and does not require additional heat treatment for activation. However, aluminosilicates sourced from natural sources require additional handling for the best use of exploitation. In this study, geopolymers were synthesized by binary use of zeolite and fly ash as main binding material and sodium silicate and sodium hydroxide as alkaline activator. The influence of alkaline activator ratios and sodium hydroxide concentrations on the compressive strength and flexural strength of the zeolite-fly ash based geopolymers were studied. In this research, zeolite-fly ash based geopolymer mortars were produced by using 50% of natural zeolite (clinoptilolite) and 50% of C-type fly ash. Four different activator ratios (Na_2SiO_3/NaOH: 1, 1.5, 2 and 2.5) and two sodium hydroxide molarities (10M and 12M) was utilized to activate zeolite and fly ash in order to determine the effect of these parameters on the mechanical strengths of the produced geopolymer mortars. The results indicated that as the alkaline activator ratio and NH molarity were increased the compressive strength of the zeolite-fly ash based geopolymers also increased. The maximum compressive and flexural strength values obtained after 28 days of curing were 20.1 MPa and 5.3 MPa respectively and corresponds when used activator ratio of 2.5 and sodium hydroxide concentration of 12 molarity. The obtained results indicated that both the alkaline activator ratio and sodium hydroxide concentration affected the compressive and flexural strengths of zeolite-fly ash based geopolymer mortar specimens.

ARTICLE INFO

Article history:
Received 4 April 2021
Revised 7 July 2021
Accepted 9 August 2021

Keywords:
Compressive strength
Geopolymer
Zeolite
Fly ash
Sodium hydroxide
Sodium silicate

1. Introduction

Geopolymer binder materials are amorphous to semi-crystalline materials that have similar structure to certain zeolitic materials which have an excellent characteristic like high strength, high fire resistance, high erosion resistance and good capability of immobilizing nuclear waste products (Van Jaarsved et al., 1999). Apart from metakaolin, some industrial waste materials like fly ash can be utilized for the production of the geopolymer materials. In the side environmental advantages, large benefits are derived by producing a new binder material with resources obtained from residue. Geopolymers which are based on aluminosilicate source materials presents a sustainable alternative for replacing Portland cement and they have been considered the cements for the future. The development of the geopolymers arose in the late of the 1970's and being fostered by work of Davidovits (Swanepoel and Strydom, 2002). Geopolymers can be produced from natural raw materials and industrial by-products that are rich in silica and alumina composition. Aluminosilicate compounds are abundant in the earth's crust and exist a large number of raw material sources rich in alumina and silicon with the ability for producing geopolymers. Among the materials which have been used for manufacturing geopolymer binder materials are fly ash (FA) (Bakharev, 2005; Xie and Xi, 2001), calcined clays (Zhang et al., 2004), blast furnace slag (Martinez et al., 2006), metakaolin (Duxson et a.l, 2007) and pozzolans (Martinez et al., 2006; Alcantara et

* *Corresponding author*. Tel.: +90-332-205-1769 ; E-mail address: oozturk@ktun.edu.tr (O. Öztürk)
ISSN: 2548-0928 / DOI: https://doi.org/10.20528/cjcrl.2021.03.003

al., 2000). Generally, alkali metals (sodium or potassium) silicate or alkali hydroxide are often used as an alkali activator for production of the geopolymer binder materials. Some of the studies estimated that producing cementitious binding materials by means of geopolymerization could result in an 86% reduction of carbon dioxide gas emissions for each ton of Portland cement (Davitovits, 2000).

The natural zeolites could be possible used as a precursors in a geopolymer synthesis (Nikolov and Rostovsky, 2017). The natural zeolite shows good pozzolanic activity when used in cement pastes (Lilkov et al., 2011) and also could add specific properties to the resulted product. Natural zeolites are hydrated aluminosilicates of alkaline and alkaline earth metals forming a group of minerals which have microporous structure based on SiO_4 and AlO_4 tetrahedrons. This property of zeolite structure is a basis for useful properties like ion exchange, selective sorption and catalytic activity (Lithareva et al., 2010).

Natural zeolite like clinoptilolite is an aluminosilicate mineral and it has been utilized as the solid source binder material when producing geopolymers. When manufacturing geopolymer pastes sand is not been used in the mix design, Villa et al. (2010) obtained compressive strength of around 30 MPa in geopolymer paste specimens when used natural zeolite (clinoptilolite) activated with sodium silicate and sodium hydroxide solutions in different proportions and cured at different temperatures. The optimum temperature range found was between 40°C and 80°C. On the other hand, Baykara et al. (2017) studied the effect of sodium hydroxide concentration, calcium hydroxide content and sodium silicate to sodium hydroxide ratios on geopolymer paste specimens when utilized natural zeolite (mordenite) and cured at various temperatures. Geopolymers of compressive strength 10 MPa after curing for 24 hours at 60°C was found. In case of manufacturing geopolymer mortars, sand is used in the mixture, Nikolov et al. (2010) produced geopolymer based on natural zeolite (clinoptilolite) and quartz sand for the synthesis of mortar using sodium hydroxide, sodium silicate and sodium carbonate as an alkali activators. The resulting geopolymer mortars showed a maximum compressive strength of 3.7 MPa after 28 days. Nikolov et al. (2017) prepared geopolymer based on natural zeolite and river sand for production of mortar using sodium hydroxide and sodium silicate as an alkali activators. Geopolymer mortars yield a compressive strength of 17 MPa after curing 28 days. Sudagar et al. (2018) studied geopolymers that contained 0%, 25%, 50% 75% replacement of metakaolin by zeolite to evaluate the compressive strength after 1, 14 and 28 days. They found the addition of zeolite in minor amounts concurrently aided in increasing the compressive strength of geopolymers.

Since zeolite is a natural pozzolan and occurs abundantly on the earth, it could provide an important opportunity to be used as geopopymer binding material and when used as partial replacement to well-known geopolymer precursors like fly ash it could provide an opportunity to decrease the amount of usage for these materials. The aim of this study was to evaluate the conditions of manufacturing of geopolymer binder materials based on natural zeolite (clinoptilolite) and C-type fly ash in order to obtain geopolymer cementitious materials that have attractive mechanical properties similar to ordinary Portland cement. In this study, 50% of natural zeolite and 50% of C-type fly ash were used to produce zeolite-fly ash based geopolymer mortars. The compressive and flexural strengths of zeolite-fly ash based geopolymer mortars were investigated considering four different sodium silicate (NS) to sodium hydroxide (NH) ratios (1, 1.5, 2 and 2.5) and two different sodium hydroxide molarities (10M and 12M). The results obtained from this study will be very useful for the application of zeolite-fly ash based geopolymers for structural purposes.

2. Experimental Stage

2.1. Materials

Natural zeolite (clinoptilolite) and C-type fly ash were used as a solid precursor to produce zeolite-fly ash based geopolymer mortars. The natural zeolite used in this study was obtained from Gordes Zeolit, Manisa, Turkey. The C-type fly ash used was obtained from Sivas Kangal Thermal Sivas, Turkey. In order to activate zeolite and fly ash, a combination of sodium silicate (NS) and sodium hydroxide (NH) solutions was used in a different silicate to hydroxide ratios. The sodium silicate solution with alkaline modulus of 1.9-2.2 and sodium hydroxide pellets were taken from a local market. The commercially available sodium hydroxide pellets with 98% purity was used and dissolved in water to produce sodium hydroxide solution with different concentrations. In this work, two sodium hydroxide concentrations (10M and 12M) and four different sodium silicate to sodium hydroxide ratios (1, 1.5, 2 and 2.5) were used. The effects of these parameters on the mechanical strengths of zeolite-fly ash based geopolymer mortars were investigated. Table 1 demonstrates the chemical composition and specific gravities of natural zeolite (NZ) and C-type fly ash (CFA) materials.

Table 1. Chemical composition and physical properties of NZ (Sevgi and Burhan, 2018) and CFA (Tahir et al., 2010).

Chemical Composition	CFA	NZ
CaO (%)	27.62	4.43
Al_2O_3 (%)	16.69	13.2
SiO_2 (%)	38.34	65.6
Fe_2O_3 (%)	5.11	1.78
MgO (%)	1.60	1.27
SO_3 (%)	4.44	0.07
Na_2O (%)	-	0.21
K_2O (%)	-	2.8
MnO (%)		0.05
Loss on ignition (%)	0.79	10.32
Specific gravity (g/cm^3)	2.3	2.41

Clean and dry river sand passing through ASTM 2 mm sieve was used as fine aggregates for this experimental study. The general gradation of the natural river sand used was provided in Table 2 and Fig. 1.

Table 2. Grading for aggregate used in this work.

Sieve Size (mm)	31.5	20	16	11.2	8	4.75	2	1	0.5	0.3	0.15	0.063
Passing Sand (%)	100	100	100	100	99.7	96.14	61.03	38.78	24.13	12.13	2	0.27

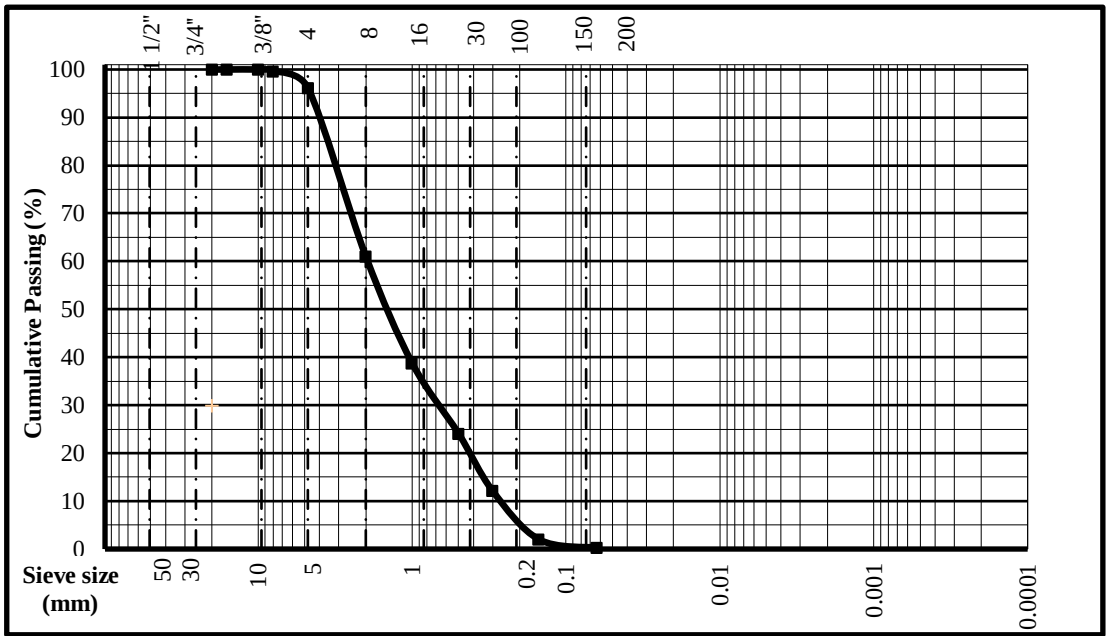

Fig. 1. Aggregate sieve analysis.

2.2. Mix Design

Table 3 shows the mix proportions of the zeolite-fly ash based geopolymer mortars with different sodium hydroxide concentrations and sodium silicate to sodium hydroxide ratios. To synthesize geopolymer mortars, water/binder was kept constant at 0.45 while activator/binder was made variable. Sand/bınder was taken 2.5 to all geopolymer mortars produced in this study. The amount extra water added to the mixture was changed according to the mixture flowability.

During mixing process, sand, zeolite and fly ash were first added in the pan mixer as a dry condition and mixed for almost 2 minutes until the mixture becomes homogeneous. Then sodium silicate and sodium hydroxide were added separately at the same time and the mixture was mixed for another 2 minutes. Finally, extra water was added into mixture and mixed for another 1 minute. The total time for mixing the raw materials was 5 minutes. For alkali activation to occur further and to enhance workability, addition of water to the geopolymer materials were reported in the past researches (Soutsos, et al., 2016).

Table 3. Mix design of zeolite-fly ash based geopolymer mortars with different molarities and sodium silicate to sodium hydroxide ratios (g).

Material	12M	12M	12M	12M	10M	10M	10M	10M
NS/NH	1	1.5	2	2.5	1	1.5	2	2.5
Natural zeolite	225	225	225	225	225	225	225	225
C type Fly ash	225	225	225	225	225	225	225	225
Sand	1125	1125	1125	1125	1125	1125	1125	1125
Sodium silicate (NS) solution	120	180	240	300	100	150	200	250
Sodium hydroxide (NH) solution	120	120	120	120	100	100	100	100
Water	202.5	202.5	202.5	202.5	202.5	202.5	202.5	202.5

*NS: Sodium silicate; NH: Sodium hydroxide

2.3. Curing conditions and testing

After the mixing process of the geopolymer mortars were finished, they were cast into the molds of size 40x40x160 mm^3 and then applied compaction using vibrating table for 72 seconds to remove entrapped airs. The geopolymer mortar samples were placed in the oven for 90 minutes, then they were removed from the oven and demolded. In this study, the samples were put into fireproof oven bags and placed in the oven at 80°C for 24 hours and then after the oven, they were left in the laboratory environment (25°C and 45% relative humidity) in a closed container until the testing day. The past studies reported that high temperature around 60 to 80°C is required to have a good compressive strength for zeolite based geopolymers (Davitovits, 2000 and Villa et al., 2010). The compressive and flexural strengths tests were prepared by using 40x40x160 mm^3 prismatic specimens according to the TS EN 196-1 standard where the geopolymer samples were test at the ages of 7, 14 and 28 days. At first stage the sample was tested for flexural strength which makes the sample into two halves. The resulting two halves were used to measure the compressive strength of the geopolymer mortar specimen.

3. Results and Discussion

3.1. Effect of 12M NH concentration on strength

Compressive and flexural strengths test results of zeolite-fly ash based geopolymer mortars with different sodium hydroxide molarities and sodium silicate to sodium hydroxide ratios (NS/NH) were given in Figs. 2-5. Figs. 2 and 3 indicate the compressive strength and flexural strength test results of zeolite-fly ash based geopolymer specimens with 12M NH concentration and different NS/NH ratios respectively. The compressive strength values of the specimens with 12M NH after 7-day curing were found to be 17.2, 17.2, 17.4 and 19.1 MPa for NS/NH ratios of 1, 1.5, 2 and 2.5 respectively. After 14 days of curing, the compressive strength values increased slight and become 18.3, 17.6, 17.9 and 19.5 MPa for the different NS/NH ratios. Finally, the compressive strength values after 28 days of curing for geopolymer mortars with 12M NH and NS/NH ratios of 1, 1.5, 2 and 2.5 are found to be 19, 18.2, 18.2 and 20.1 respectively.

Flexural strength values of the specimens with 12M NH also show a linear increase after curing 7 days. As shown from Fig. 3, flexural strength values for geopolymer mortars with 12M NH and NS/NH ratios of 1, 1.5, 2 and 2.5 at 7 and 14 days were 4.5, 4.6, 4.6, 5.2 MPa and 4.3, 4.2, 4.9, 5.2 MPa respectively. Finally, flexural strength values after 28 days of curing for geopolymer mortars with 12M NH and NS/NH ratios of 1, 1.5, 2 and 2.5 were found to be 5.2, 4.8, 5.1 and 5.3 respectively.

3.2. Effect of 10M NH concentration on strength

Figs. 4 and 5 show the compressive strength and flexural strength test results for geopolymer mortar specimens with 10M NH concentration and NS/NH ratios of 1, 1.5, 2 and 2,5 respectively. The compressive strength values passed 17 MPa for geopolymer mortars with NS/NH ratios of 1.5, 2 and 2.5 while the compressive strength values of the geopolymers with low NS/NH ratio of 1 reached around 12 MPa. The results pointed out that the compressive strength values for the geopolymer mortar specimens with 10M NH concentration were found to be increased when the alkaline activator ratio was increased. The compressive strengths of the geopolymer mortars slightly increased with increasing curing period. For NS/NH ratio of 2.5, the compressive strength values increased 16.4 MPa for 7 days to 17.9 MPa for 28 days of curing period. The highest flexural strength values for geopolymer mortar specimens with 10M NH concentration reached 5.2 MPa when the NS/NH ratio was 2.5. Fig. 5 shows that some of the flexural strength values slightly decreased with curing period. For NS/NH ratio of 2.5, the flexural strength reached maximum of 5.2 MPa for 7 days of curing and decreased to 5.1 MPa for 28 days of curing.

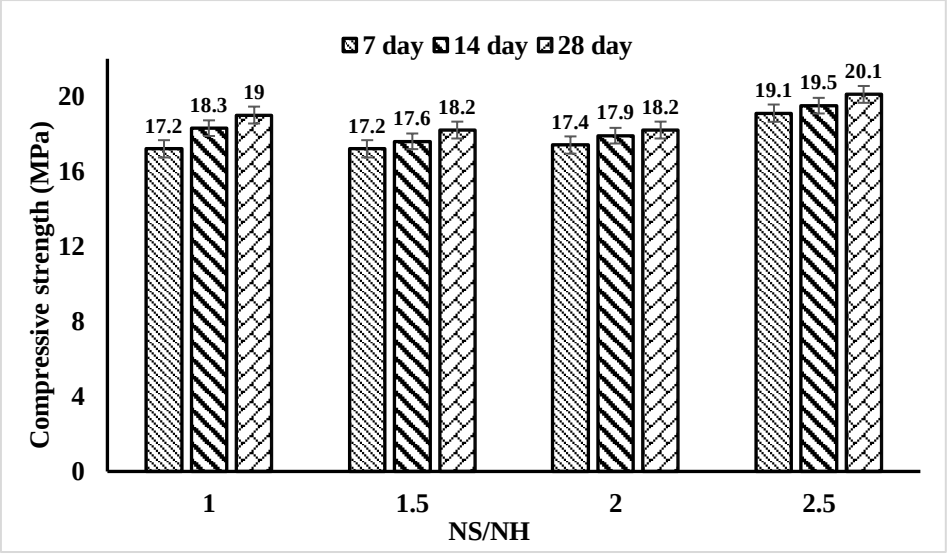

Fig. 2. Compressive strength values with 12M NH after 7, 14 and 28 days.

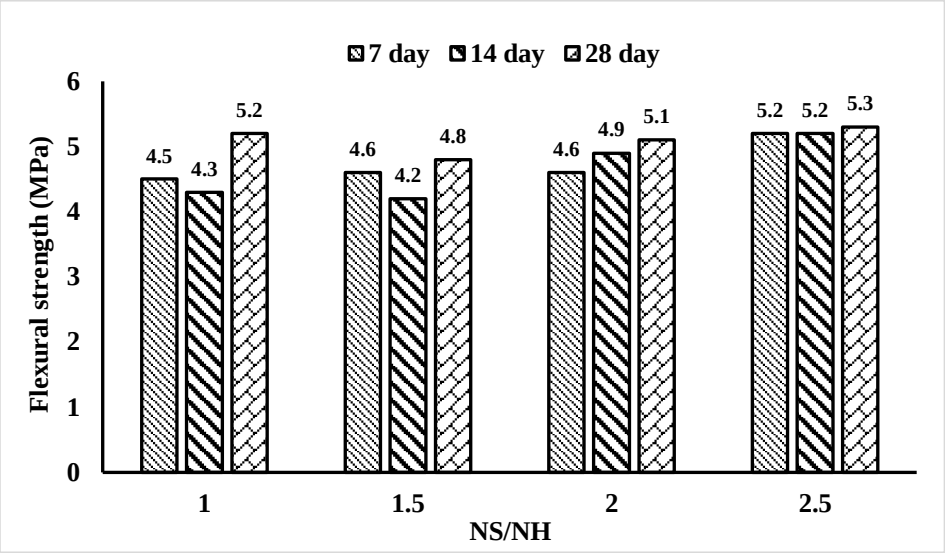

Fig. 3. Flexural strength values with 12M NH after 7, 14 and 28 days.

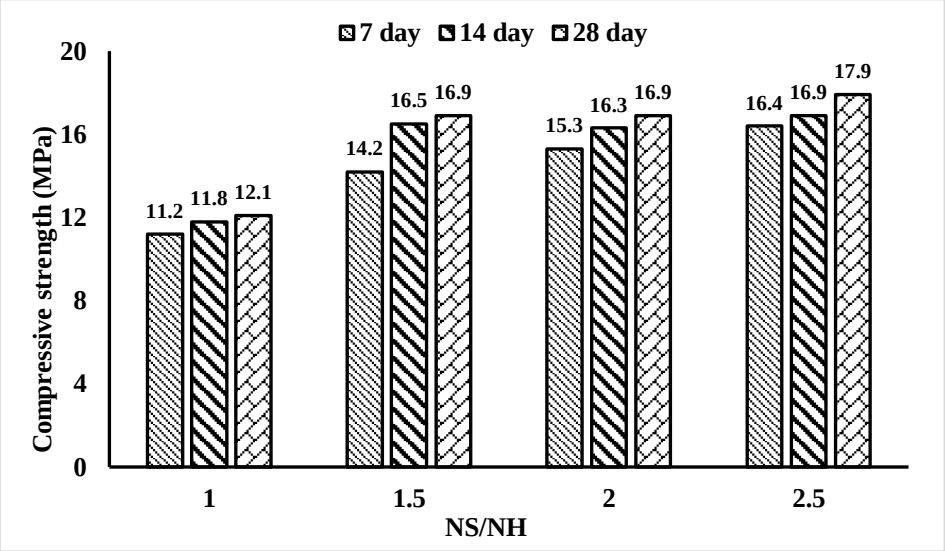

Fig. 4. Compressive strength values with 10M NH after 7, 14 and 28 days.

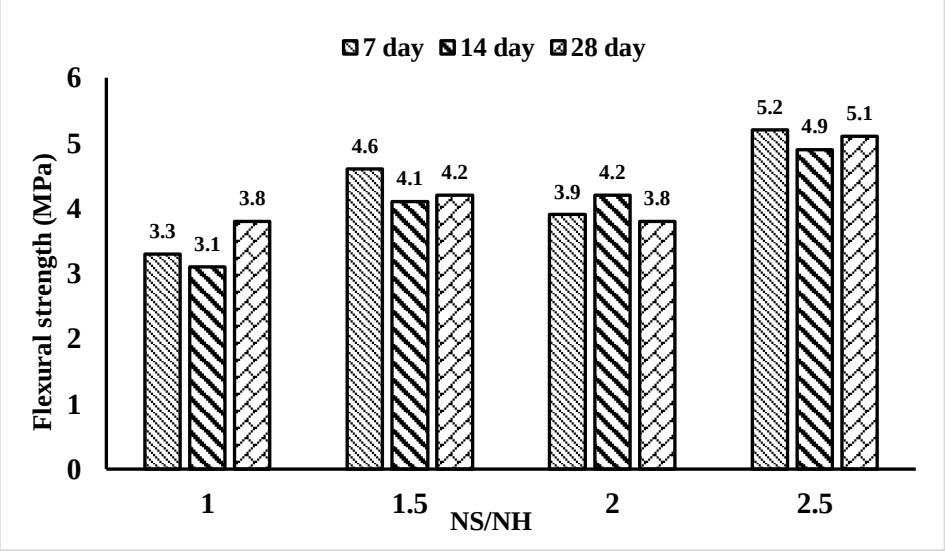

Fig. 5. Flexural strength values with 10M NH after 7, 14 and 28 days.

3.3. Effect of alkaline activator ratios on strength

Figs. 6 and 7 show the influence of alkaline activator (NS/NH) ratios on the compressive and flexural strengths of the zeolite-fly ash geopolymer mortars with different NH concentration molarities. The compressive strength values of the geopolymer mortars with 10M NH molarity increased from 12.1 MPa to 17.9 MPa for 28 days of curing period when NS/NH ratios increased from 1 to 2.5. However, the compressive strength values of the geopolymer mortars with 12M NH first reached 19 MPa when NS/NH ratio was 1 and finally reached maximum value of 20.1 MPa when NS/NH ratio 2.5.

As Fig. 7 indicates, the flexural strength values of the geopolymer mortars with 10M NH molarity for 7 days of curing increased from 3.3 MPa to 5.2 MPa when NS/NH ratios increased from 1 to 2.5. The flexural strengths increased from 3.8 MPa to 5.1 MPa when NS/NH ratios increased from 1 to 2.5 for 28 days of curing. For geopolymer mortars with 12M NH molarity, the flexural strengths increased from 4.5 MPa to 5.2 MPa when NS/NH ratios increased from 1 to 2.5 for 7 days of curing. Finally, the flexural strengths of geopolymer mortars with 12M NH molarity increased slightly from 4.3 MPa to 5.3 MPa for 28 days of curing when NS/NH increased from 1 to 2.5.

For the comparison of the utilized alkaline activator ratios, the compressive strength values of the specimens with different NH concentrations for different curing periods are given in Table 4.

The results pointed out that the maximum compressive strength was obtained in the specimens with a NS/NH ratio 2.5 and NH concentration of 12M, while the minimum compressive strength was achieved on the specimens with a NS/NH ratio of 1 and 10M NH concentration. A maximum compressive strength of 17 MPa for only zeolite geopolymer mortar specimens with a NS/NH ratio of 2.5 was also obtained in the study of Ulloa et al. (2018). In addition, the compressive strength values of the zeolite-fly ash geopolymer mortar specimens with 12M NH concentrations increased with the curing period.

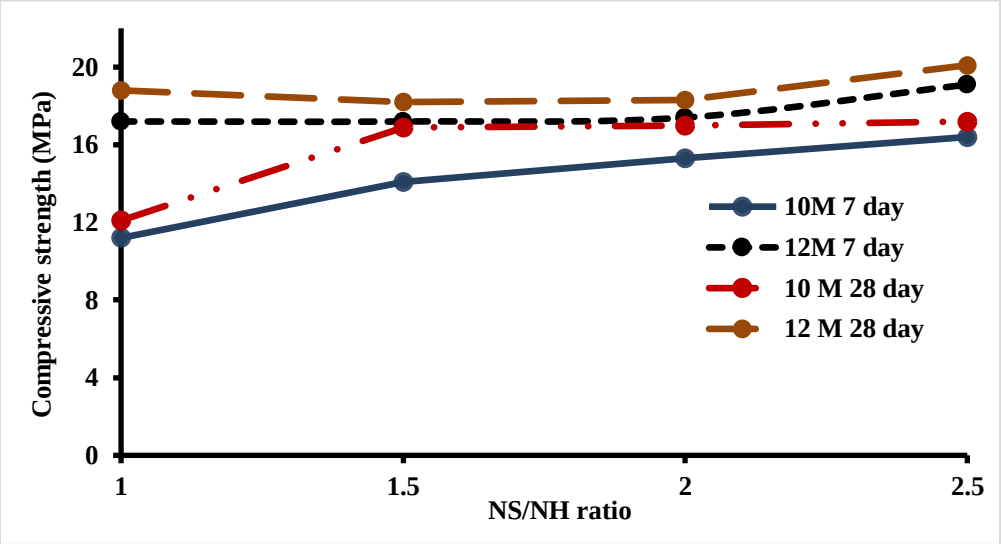

Fig. 6. Compressive strength values of geopolymers with various alkaline activator ratios.

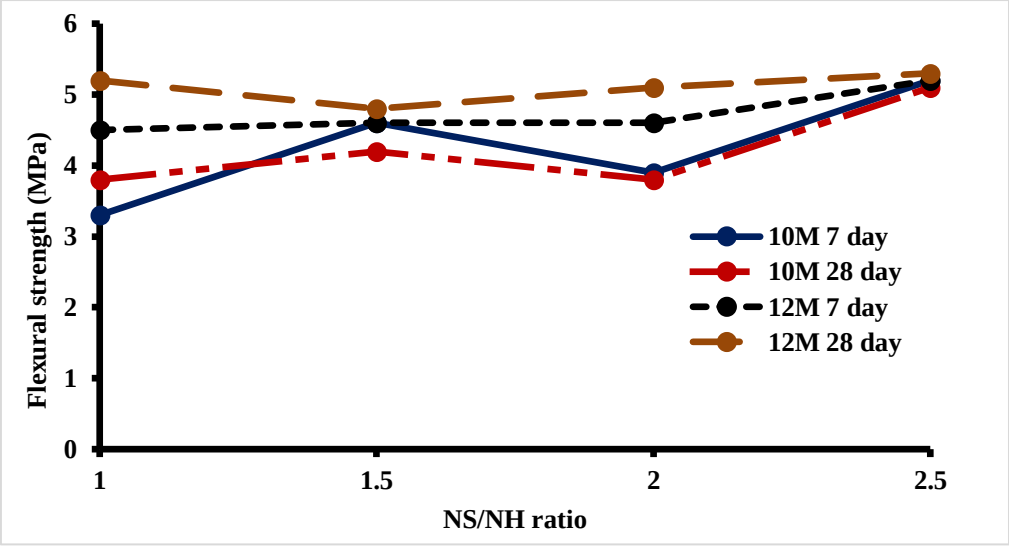

Fig. 7. Flexural strength values of geopolymers with various alkaline activator ratios.

Table 4. Compressive strength values for geopolymers produced in this study.

NS/NH ratio	10M 7 day	10M 14 day	10M 28 day	12M 7 day	12M 14 day	12M 28 day
1	11.2	11.8	12.1	17.2	18.3	19
1.5	14.2	16.5	16.9	17.2	17.6	18.2
2	15.3	16.3	16.9	17.4	17.9	18.2
2.5	16.4	16.9	17.9	19.1	19.5	20.1

4. Conclusions

In this study, effect of two different sodium hydroxide concentrations (10M and 12M) and four various alkaline activator (sodium silicate/sodium hydroxide) ratios (1, 1.5, 2 and 2.5) on the mechanical strengths (compressive and flexural strengths) of zeolite-fly ash based geopolymer mortar cured under ambient temperature for 7, 14 and 28 days were investigated. The results of the experimental study are summarized as follows:

- The compressive strength values of the geopolymer mortar specimens were mostly influenced by the alkaline activator (NS/NH) ratio and sodium hydroxide (NH) concentrations while curing periods applied to the geopolymer mortars slightly influenced the compressive strength values. For the specimens with 12M NH concentrations, the compressive strength values increased from 17.2 to 19.1 MPa for 7 days, from 18.3 to 19.5 MPa for 14 days and from 19 to 20.1 MPa for 28 days of curing for different NS/NH ratios.
- The compressive strength values of the geopolymer mortars produced by using 10M NH were smaller than that of 12M NH. The compressive strength values of the geopolymer specimens with 10M NH concentrations increased from 11.2 to 16.4 for 7 days, 11.8 to 16.9 MPa for 14 days and 12.1 to 17.9 MPa for 28 days of curing period for different NS/NH ratios. From this observation, it can be concluded that as the amount of NH in the mixture increase, the compressive strength of the geopolymer mortars showed an increase.
- The compressive strength values for the geopolymer mortar specimens with different sodium hydroxide concentrations were found to be increased when the alkaline activator ratio was increased. The maximum compressive strength of 20.1 MPa was obtained when used an activator ratio of 2.5 while the minimum compressive strength of 11.2 MPa was obtained when used an activator ratio of 1.
- For the specimens with 12M NH concentrations, the flexural strength values increased from 4.5 to 5.2 MPa for 7 days, from 4.3 to 5.2 MPa for 14 days and from 5.2 to 5.3 MPa for 28 days of curing for different NS/NH ratios. While the flexural strength values of the geopolymer specimens with 10M NH concentrations increased from 3.3 to 5.2 for 7 days, 3.1 to 4.9 MPa for 14 days and 3.8 to 5.1 MPa for 28 days of curing period for different NS/NH ratios.
- The flexural strength values of the geopolymer mortar specimens with 12M NH concentration were found to be higher than that of 10M NH concentration.
- The flexural strength of 12 M NH geopolymer mortars showed a linear increase when the alkaline activator ratios was increased. While flexural strength of 10M NH geopolymer mortars behaved differently from 12M NH geopolymer mortars. The flexural strength of 10M NH geopolymer mortars first show an increase from activator ratio of 1 to 1.5 and then the flexural strength showed a decrease when activator ratio increases from 1.5 to 2 and finally the flexural strength showed an increase again when activator ratio increased from 2 to 2.5.

References

Alcantara E, Cheeseman Ch, Knight J, Loizidou M (2000). Properties of alkali activated clinoptilolite. *Journal of Cement and Concrete Research*, 30, 1641-1646.

Bakharev T (2005). Geopolymer materials prepared using class F fly ash and elevated temperature curing. *Journal of Cement and Concrete Research*, 35, 1224-1232.

Baykara H, Cornejo MH, Murillo R, Gavilanes, A, Paredes C, Elsen J (2017). Preparation, characterization and reaction kinetics of green cement: Ecuadorian natural mordenite based geopolymers. *Materials and Structures*, 50, 188.

Davitovits J (1991). Geopolymers: inorganic polymeric new materials. *Journal of Thermal Anal*, 37, 1633-1656.

Duxson P, Mallicoat SW, Lukey GC, Kriven WM, van Deventer JSJ (2007). The effect of alkali and Si/Al ratio on the development of mechanical properties of metakaolin-based geopolymers. *Colloids and Surfaces A: Physicodhem. Eng. Aspects*, 292, 8-20.

Lilkov V, Petrov O, Petkova V, Petrova N, Tzveyanova Y (2011). Study of pozzolanic activity and hydration products of cement pastes with addition of natural zeolites. *Journal of Clay Minerals*, 46(2), 241-250.

Lithareva N, Dimova L, Petrov O, Tzvetanova Y (2010). Ag+ sorption on natural and Na-exchanged clinoptilolite from Eastern Rhodopes, Bulgaria. *Journal of Microporous and Mesoporous Materials*, 130(1), 32-37.

Martinez-Ramirez S, Blanco-Varela MT, Erena I, Gener M (2011). Pozzolanic reactivity of zeolitic rocks from two different Cuban deposits: characterization of reaction products. *Journal of Applied Clay Science*, 32, 40-52.

Nikolov I, Rostovsky I (2017). Sodium-silicate geopolymers based on natural zeolite-clinoptilolite. *Comptes rendus de l' A bulgare des sciences*, 70, 1655-1662.

Nikolov A, Rostovsky I, Nugteren H (2017). Geopolymer materials based on natural zeolite, case study. *Construction and Building Materials*, 6, 198-205.

Sevgi O, Burhan A (2018). Compressive strength and microstructural characteristics of natural zeolite-based geopolymer. *Periodica Polytechnica Civil Engineering*, 68, 64-71.

Soutsos M, Boyle AP, Vinai R, Barnett SJ (2016). Factors influencing the compressive strength of fly ash based geopolymers. *Construction and Building Materials*, 110, 355-368.

Sudagar A, Andrejkovicova S, Patinha C, Velosa A, McAdam A, Ferreira da Silva E, Rocha F (2018). A novel study on the influence of cork waste residue on metakaolin-zeolite based geopolymers. *Journal of Applied Clay Science*, 152, 196-210.

Swanepoel JC, Strydom CA (2002). Utilization of fly ash in geopolymeric materials. *Applied Geochemistry*, 17, 1143-1148.

Tahir G, Salih Y, Nusret B (2010). High temperature resistance of self-compacting lightweight concrete with pumice aggregate. *Gazi University Engineering and Architecture Journal*, 3, 459-467.

TS EN 196-1 (2016). Method of testing cement-Part 1: determination of strength. Turkish Standards Institute, Ankara, Turkey.

Ulloa NA , Baykara H, Cornejo MH, Regail A, Paredes C, Villalba JL (2018). Application-oriented mix design optimization and characterization of zeolite-based geopolymer mortars. *Construction and Building Materials*, 174, 138-149.

Van Jaarsved JGS, Van Deventar JSJ, Schwartzman A (1999). The potential use of geopolymer materials to immobilize toxic metals: Part II. Material and leaching characteristics. *Journal of Material Engineering*, 12, 75-91.

Villa C, Pecina ET, Torres R, Gomez L (2010). Geopolymer synthesis using alkaline activation of natural zeolite. *Construction and Building Materials*, 24, 2084-2090.

Xie Z, Xi Y (2001). Hardening mechanisms of an alkaline activated class F fly ash. *Journal of Cement and Concrete Research*, 31, 1245-1249.

Zhang S, Gong K, Lu J (2004). Novel modification method for inorganic geopolymer by using water soluble organic polymer. *Journal of Material Letters*, 58, 1292-1296.

Challenge Journal of Concrete Research Letters

Research Article

Effect of retardant admixtures type and their using method on the behavior of concrete

Tamer Ibrahim Ahmed [a,*], Mohamed Roshdy Afify [b]

[a] *Department of Civil Engineering, Higher Institute of Engineering and Technology, Kafr el-Sheikh, Egypt*
[b] *Department of Civil Engineering, Menoufia University, Shebin ElKoum, Menofia, Egypt*

ABSTRACT

Construction sites may be exposed to crisis conditions during the casting process, resulting in delays of several hours and causing destruction of ready-mix concrete. This study suggests an experimental analysis of the possibility of using a specific additional dose of retardant admixtures, which may be used to ready-mix concrete before the initial setting of the concrete occurs. The effect of this additional dose on concrete characteristics in terms of workability, setting time, and compressive strength is also being studied. To conduct this investigation, three types of retardant admixtures from three branded companies were used. In addition, a penetration resistance experiment was conducted on the concrete to determine its setting time. The setting time of concrete was measured at different period intervals depending on when the additional dose of the retardant admixtures was added from the start of the concrete mixing. The results showed that concrete maintained proper workability for a period of more than five hours after using the additional dose of retarding admixtures. The additional dose of retarding admixtures not only delayed the concrete setting but also improved the compressive strength of the concrete. This implies that the use of an additional dose of retardant admixtures specifically tailored for ready-mix concrete is an effective option to avoid the return of ready-mixed fresh concrete.

ARTICLE INFO

Article history:
Received 2 June 2021
Revised 7 July 2021
Accepted 10 August 2021

Keywords:
Retardant admixtures
Compressive strength
Setting time
Additional dose
Penetration resistance

1. Introduction

Concrete is a main objective for building development and infrastructural progress all over the world as a result of its durability, strength, and being economical (Esfahani et al., 2021).

Admixtures are natural or manufactured chemicals or additives added during concrete mixing to enhance specific properties of the fresh and hardened concrete (Blankendaal et al., 2014). The use of admixtures in concrete allowed for increased workability and strength without raising the cement content or requiring more water. Retardant admixtures are used to slow down the setting time and to improve the primary flow capacity (Rohden et al., 2012). The output of the retardant relies on the chemical and mineralogical configuration of the cement and the content of admixtures (Belous et al., 2009). Lignosulfonic acids and their salts, hydroxyl-carboxylic acids and their salts, inorganic salts, phosphates and sugars and their derivatives are the major sources of materials, which form retardant compounds (Neville, 2013).

Several researchers have studied the factors that influence the behavior of the retardant admixtures through the hydration process, such as the cement form, the retardant form, the retardant quantity, and the temperature degree through adding the admixtures to the concrete (Khan, 2004). Ozturk and Baradan (2011) studied the impact of the form and excess dose of retardant admixtures on certain mechanical and microstructural properties of cement mortar. Results exhibited that cement mortars with retardant admixtures had greater strength rates by making a more normal microstructure with reduced porosity. Islam et al. (2019) examined the effect of the retarding super plasticizer on the workability

* *Corresponding author*. Tel.: +2-01-017-430601 ; Fax: +2-04-082-197784 ; E-mail address: tamerib93@gmail.com (T. I. Ahmed)
ISSN: 2548-0928 / DOI: https://doi.org/10.20528/cjcrl.2021.03.004

of cement past, mortar, and concrete. The results showed that the workability of all mixtures was improved by the use of super plasticizers from different manufacturers. The results also determined that the properties of cement paste, mortar and concrete could be enhanced with the ideal dosage for each type of admixture. Alsadey (2013) investigated the effects of super plasticizer and retarder on the properties of concrete with a specific strength of 30 MPa. The results showed that the workability of concrete could be improved by adding a super plasticizer and a retarder.

Kubissa et al. (2021) investigated the effect of an air entraining admixture and citric acid as concrete setting retarder on concrete durability. The findings obtained indicated that citric acid applied at 0.2% of the cement weight clearly increased concrete's durability parameters and also decreased water absorption and air permeability. By incorporating an air entraining admixture, the opposite effect was achieved. The combined use of both additives led to an interaction between them, whose results were varied and dependent.

Souza et al. (2020) considered the role of chemical admixtures in producing large-scale buildings by 3D printed concrete. Results showed that chemical admixtures improved the fresh concrete rheological criteria, setting the desired quality, and preserving for longer periods the workability and build ability. Rohden et al. (2012) investigated the influence of chemical admixture form and dose mortar's on the mechanical properties of concrete. Results revealed that compressive strength values rose from 2% to 6% and flexural strength values rose from 1% to 6% due to the use of chemical admixtures.

In the field of concrete construction awareness of the setting characteristics of concrete is essential. It would help to plan the different stages involved in concrete building operations such as transportation, installation, compaction and concrete finishing (Brooks et al., 2000). Gnanaraj et al. (2020) investigated the effects of various mineral admixtures and chemical additives used in self-compacting concrete, as well as the changes in mechanical behavior caused by these admixtures. The outcomes showed that the use of a mineral additive such as rice husk ash increased the mechanical qualities of self-compacting concrete by up to 15% when compared to standard Portland cement. However, it was shown to have a highly flowable matrix with little chloride ion resistance. Fernandes and Guptha (2021) investigated the impact of recent chemical admixtures on the strength of cement mortar cubes. In comparison to the cubes evaluated without any admixtures, it was established that the inclusion of admixtures did not give excellent performance in the strength of mortars.

Researchers are looking for different ways to reduce the amount of fresh ready-mixed concrete returned, which has a negative impact on the environment and on the economy (Obla et al., 2007; Gonzalez et al., 2004; Suresh et al., 2016). To characterize the unused concrete returned to the truck facility, it was divided into 60%, which went directly to the landfill site. The remaining 40% was used to manufacture various products of concrete or recycled materials (Ferrari et al., 2014). Negasie et al. (2019) studied the properties of concrete made from mixing returned fresh mixture of concrete mixed with natural and retarded ready-mix concrete. The results showed acceptable values for workability, setting time, and compressive strength of concrete.

This paper investigates the effect of three types of retarding admixtures on the performance of concrete. Retarding admixtures from three branded companies were used to help concrete to remain fresh for a longer time. Nine mixtures were made with retardant admixtures, either once at the beginning of the mixing or by using a second additional dose of retardant admixtures at different times after mixing. The properties of those mixtures were compared with a control mixture that did not contain retardant admixtures. In terms of value, the determination of the concrete setting time was more important and necessary than the determination of the cement-setting time for construction workers. Penetration resistance monitoring was applied in several studies to assess the setting time of specific suspicion (Brooks, 2000; Suresh et al., 2016). The setting time of concrete in this study was measured by penetration resistance for all mixtures, as well as assigning workability and compressive strength to all mixtures.

2. Experimental program

2.1. Materials

Ordinary Portland cement (OPC), natural siliceous sand as a fine aggregate, gravel as a coarse aggregate and retardant chemical compounds have been used in this study. Class 42.5 N OPC meets the requirements of (E.S. 4765-1, 2012). The specific gravity and Blain fineness of OPC were 3.15 g/mm^3 and 3986 cm^2/g, respectively. Gravel with size 10 mm and sand were collected from Suez zone. Physical properties of used aggregates are described in Table 1. The particle size distribution of used aggregates shown in Fig. 1.

Potable water was used with no strange taste, color bouquet, or turbidity. Three types of retardant admixtures have been collected from three branded companies. The first admixture was (Plastimnt -AR340) collected from Sika, the second was (Addicrete BVSS-CMB) collected from CMB and the third was (Techno-mix 130 CR) collected from (MTC) company. The three admixtures were characterized by a dark brown color. Their relative density was about 1.1 ± 0.005 kg/L. The content of chloride was not more than 0.2%. The chemical compounds of the tree admixtures are shown in Table 2.

Table 1. Physical properties of fine and coarse aggregates.

No.	Property	Value	
		Sand	Gravel
1	Specific gravity	2.58	2.65
2	Bulk density (kg/m^3)	1555	1632
3	Fineness modulus	2.72	5.6
4	Absorption (%)	1.2	0.9

Table 2. Different components of used admixtures.

Component for retarding	in "Addicrete BVSS-CMB"	in "Plastimnt -AR340"	in "Techno-mix 130 CR"
Glucose polymers	5%	4%	7%
Salts of lignosulfonic acid	80%	82%	78%
Salts of hydroxylases carboxylic acids	15%	14%	15%

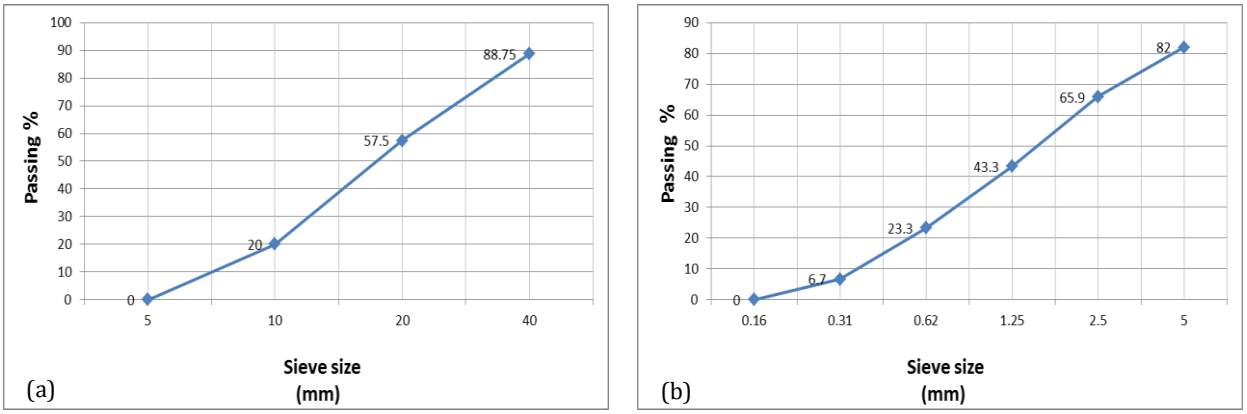

Fig. 1. Particle size distribution of used aggregates: (a) Sieve analysis for sand; (b) Sieve analysis for gravel.

3. Experimental Methodology

The impact of different types of retardant admixtures and how they're used on concrete behavior was studied. For this purpose, the effect of using three various types of retardant admixtures on ready -mix concrete has been studied at different periods since the beginning of the mixing process. The methodology included in this investigation was subdivided into two parts. Workability and setting time were performed in the first phase of the preliminary tests. The strength of specimens was evaluated in the second stage.

To determine the setting time for fresh concrete in this research, the penetration resistance test was applied in accordance with (ASTM C09, 2008). The concrete mixes were designed according to the ACI method (ACI 211.1-91, 1991) with a required compressive strength of 32 N/mm^2 and using a constant water/cement content of 0.4. Ten mixtures were prepared and 12 cubes 150x150x150 mm were cast for each mixture, with a total of 120 cubes. The mixture components of ten mixes are described in Table 3.

After casting and leveling the surface of the cubes, the front of the penetration tool was inserted on regular occasions to determine the force necessary for penetration as shown in Fig. 2. The concrete implantation process has been repeated and the relationship has been established between the reaction of the penetration device resistance and the time taken to reach the required values to achieve the initial and the final setting time of each mixture used in this study. The values of concrete setting time were recorded when the penetration resistance value was 3.5MPa (500 psi) as the initial setting occurred. The final setting was also reported when the resistance to penetration exceeded 27.5 MPa (4000 psi) (Suresh et al., 2016).

The first mixture was prepared without using any retardant admixtures and mentioned as the control mixture for the rest mixtures and symbolized by (CN0). The symbol (CN) indicated the mixture name and the number (0) indicated that it contained no retardant admixtures. The remaining nine mixtures which contained different retardant admixtures were classified into three groups, with three mixtures in each group. The first group of mixtures in which the three types of retardant admixtures were used only once at the beginning of the mixing process were symbolized by (AD1, BD1, and CD1). The symbol (AD) indicated the first admixture (Plastimnt -AR340) collected from Sika, the symbol (BD) refers to the second admixture (Addicrete BVSS) collected from CMB and the symbol (CD) refers to the third admixture (Techno-mix 130 CR) collected from (MTC) company. The number (1) designated that the three retardant admixtures were used only once in the mix and their addition time was at the start of mixing. The quantity of retardant admixtures used at the beginning of the mixing process according to mix design was 6.8 kg/m^3. The setting time of concrete for all mixtures of the first group and control mixture was determined before the preparation of the second and third group mixtures. The second group of mixtures whose symbols were (AD2M, BD2M, and CD2M) and the retardant admixtures were used twice, the first at the beginning of the mixing process and the second after some time equal to the middle of the initial setting time calculated using the penetration resistance device. Number (2) was added to the symbols of the mixtures of the second and third groups to indicate the use of the retardant admixtures two times during the preparation of samples.

The symbol (M) expresses the timing of the second additional dose being used after duration equal to the middle of the initial setting time which was measured beforehand.

The third group of mixtures whose symbols were (AD2H, BD2H, and CD2H) that retardant admixtures were used twice as well, the first at the beginning of the mixing process and the second at a period equal to half an hour before the pre-calculated initial setting time occurred. The symbol (H) indicated the timing of the second additional in the third group mixtures. The quantity of the additional dose of admixtures added for the second time was 1.7 kg/ 1m^3 which present 25% from the amount of admixtures used at the start of the mixing process. After the completion of the preparation of the mixtures of the third group, the time of setting was calculated for them in the same way for the first and second group's mixtures using the penetration resistance device. The workability test was determined and the compressive strength was examined for all samples used. The slump test was performed to evaluate the workability according to (ASTM C143, 2015). The slump test was performed for all mixtures used in the study at different times from the start of mixing and every an hour passed.

In accordance with the specifications, a 2000 kN compression machine was used to measure the compression of concrete cubes with a size of 150x150x 150 mm at 7 days, 28 days, 56 days, and 90 days of age. A series of three cubes was tested for every mix and the average rate of these three cubes was re-counted as a result. All cubes were cured with water before the test day.

Fig. 2. Penetration resistance test proceeding.

Table 3. Mix proportion details of ten mixes/1 m^3.

Mixes codes	Cement (kg)	Sand (kg)	Gravel (kg)	Water content (liter)	Admixture content (liter)	Admixture type	Number of using admixture in mixes
CN0	400	776	1154	160	--	--	--
AD1	400	776	1154	160	6.8	Plastimnt -AR340-Sika	1
BD1	400	776	1154	160	6.8	Addicrete BVSS-CMB	1
CD1	400	776	1154	160	6.8	Techno-mix 130 CR	1
AD2M	400	776	1154	160	8.5	Plastimnt -AR340-Sika	2
BD2M	400	776	1154	160	8.5	Addicrete BVSS-CMB	2
CD2M	400	776	1154	160	8.5	Techno-mix 130 CR	2
AD2H	400	776	1154	160	8.5	Plastimnt -AR340-Sika	2
BD2H	400	776	1154	160	8.5	Addicrete BVSS-CMB	2
CD2H	400	776	1154	160	8.5	Techno-mix 130 CR	2

4. Results and Discussions

4.1. Workability

The workability of all mixtures used in this study was assessed. The slump test was used to assess the workability of all mixtures. Table 4 presents the findings of slump value analysis for all used mixes. The slump was measured at the beginning of the mixing process and was re-measured at each passing hour.

Table 4 shows all workability measurement results for all mixtures using the slump test. The slump values for the control mixture (CN0) have decreased with the passage of time due to the occurrence of concrete hardening over time. The results showed that the use of retardant admixtures enhanced the workability by increasing the slump values for first-group mixtures containing retardant admixtures (AD1, BD1, and CD1) by average percentages of 14.3%, 7.7%, and 11.11%, respectively, relative to the reference mix (CN0) for the three types of admixtures used. This increment was due to the presence of retardant admixtures which slowed down the process of hardening concrete (Borahan et al., 2018). This result indicated that the mixtures continued to maintain a degree of workability due to the use of retarding admixtures at the beginning of casting. These results are consistent with what was obtained by Fernandes and Guptha (2021).

With respect to the second group of mixtures (AD2M, BD2M, and CD2M), the slump values varied with the use of retardant admixtures at the start of the mixing process and after the addition of the second dose at a time equal to the middle of the setting time of mixtures (AD1, BD1, and CD1). It was found that after 180 min from the start of the mixing process, the second group of mixtures recovered their ability to work and consistency, where the mixture slump values were 90 mm, 85 mm, and 80 mm, which was higher than the control

mixture slump values after only one hour by 11.1%, 5.9%, and 12.5% respectively, as shown in Fig. 3. The slump values for the three mixtures were still suitable even after 300 min, allowing for casting, compaction, and leveling of concrete operations to be done without any hindrance. However, when using an additional dose of retardant admixtures at a time equal to the middle of the initial setting time, the concrete started to restore its workability again due to the availability of a liquid medium. Admixtures also worked, in addition to reducing friction between the concrete particles formed, which helped increase the slump values again.

Table 4. Slump values for all mixtures used.

Mixes codes	At 0 min (Batching)	After (60 min)	After (120 min)	After (180 min)	After (240 min)	After (300 min)
CN0	120	80	45	--	--	--
AD1	140	80	70	60	40	--
BD1	130	70	60	50	30	--
CD1	135	75	65	55	45	--
AD2M	160	120	85	90	75	55
BD2M	155	115	80	85	70	50
CD2M	150	110	75	80	60	45
AD2H	155	120	85	40	25	30
BD2H	150	110	80	35	22	25
CD2H	150	105	75	35	20	24

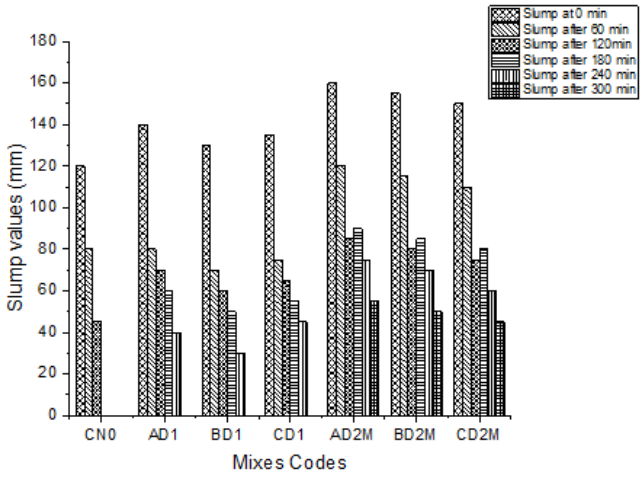

Fig. 3. Comparison between slump values of first and second groups mixtures with control mixture.

For the third group of mixtures (AD2H, BD2H, and CD2H), retardant admixtures were also used at batching, and then an additional second dose was used half an hour before the initial setting time occurred. The behavior of the mixtures did not cause a significant change, as with the passage of time, the slump values began to decrease because of the hardening of the concrete. Semi-temporary hardening of the hardening process occurred with the use of the second additional dose of admixtures half an hour before the initial setting time occurred, but it did not help to increase the concrete slump values and therefore did not improve the workability of the mixtures. Whereas after 300 min from the start of mixing, the values of slump of mixtures of the third group were 30, 25 and 24 mm, which was less than the values of slump of mixtures of the first group at the same time by 40%, 50% and 20%, respectively, as shown in Fig. 4. This result happened because most of the concrete particles lost their ability to form due to the passage of time and the occurrence of chemical reactions during the hardening process.

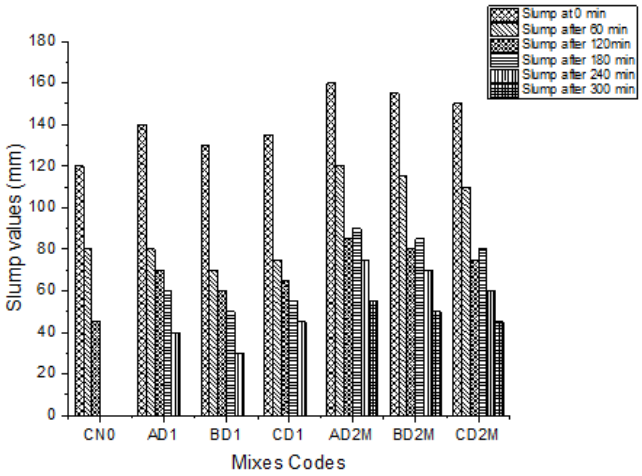

Fig. 4. Comparison between slump values of first and third groups mixtures with control mixture.

From these results, the positive influence of the additional dose of retardant admixtures was seen for a second time after a duration equal to the middle-term of the measured mixture-setting term of the first group (AD1, BD1, and CD1). This was because the use of the admixtures slowed down the occurrence of the hardening process for the first time when the mixture occurred. With the passage of time, the workability began to decrease, and with the addition of retardant admixtures again, the mixture recovered its workability according to the second addition, which facilitates the slipping of aggregates and cement granules. A liquid medium, which facilitated

mixing and freedom of movement, was also given. With respect to the third group, in which the second additional dose was used half an hour before the initial setting time occurred, a continuation of declining slump values with the passage of time was observed and there was no noticeable increase in workability when the second addition of retardant admixtures was used, indicating that the hardening process had reached a stage that the mixtures could not handle. The second dose of admixtures at a time equal to half an hour before the initial setting time occurred did not help to slow down effectively, as was the case when the retardant admixtures were used at a time equal to the half-time of the calculated setting time for the mixtures used.

4.2. Setting time

In this study, the focus was on determining the setting time for concrete, since it was more important than estimating the setting time for cement. Because of the chemical reaction between cement components such as C3S and C3A with water, concrete setting occurs, and with the passing of time, the concrete becomes an increasing amount of hard and its surface resistance increases the strength of the penetrator arm. Table 5 displays the measurements of the initial and final setting time of all mixtures used. For mixes of the first group, the initial setting time was measured immediately after mixing and sample preparation. As a result, the setting time values for the control mixture using the penetration resistance apparatus have been found to be within their normal range. A significant difference in initial and final setting values occurred with the use of retardant admixtures in the first group of mixtures. The retardant admixtures delayed the initial setting time of the mixtures of the first group by 50%, 49%, and 48% compared to the initial setting time of the control mixture and delayed their final setting time by 34%, 31.96%, and 30.53% compared to the final setting time of the control mixture, as shown in Fig. 5. The presence of retardant admixtures slowed down the process of concrete hardening, allowing setting time to increase.

Table 5. Initial and the final setting time values for all mixtures by penetration resistance device.

Mixes codes	Initial setting time (min)	Final setting time (min)
CN0	130	330
AD1	260	500
BD1	255	485
CD1	250	475
AD2M	370	710
BD2M	360	690
CD2M	350	680
AD2H	300	560
BD2H	290	545
CD2H	285	540

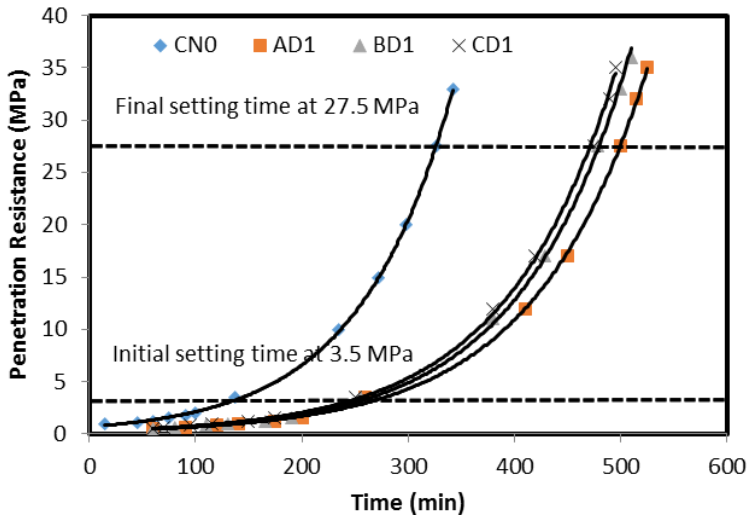

Fig. 5. Initial and the final setting time values for control mix and first group mixtures.

For mixtures of the second and third groups, the setting time was measured for them after adding the second dose of retardant admixtures according to the time of addition for each group. For the second group mixtures (AD2M, BD2M, and CD2M), the second addition was added after some time equal to the middle of the

calculated initial setting time of mixtures (AD1, BD1, and CD1).With the addition of the second dose of retardant admixtures to the second group mixtures, their initial and final setting time delayed by 27.8%, 25%, and 24.2 compared to the initial setting time of the first group mixtures and delayed by 29.6%, 29.7%, and 30.1% compared to the final setting time of the first group mixtures, as shown in Fig. 6. The chemical reaction between the concrete components and the water began from the first moment of mixing; the continuous mixing of materials until the second dose of retardant admixtures was added helped to further reduce in the rate of concrete hardening. The act of retarder admixture delayed the direct hydration of C3A, decreasing the initial setting time (Belous et al., 2009). The timing of the second dose addition was also an important factor in increasing the setting time that helped to keep concrete in fresh condition. The use of a second extra dose of retardant admixtures in the middle of the setting time was appropriate to avoid strong bonding between concrete components, which helped to keep concrete in fresh condition for a while.

For the third group mixtures (AD2H, BD2H, and CD2H), the second addition was added at time equal to half an hour before the initial set of mixtures occurred based on the set time measured for the mixtures (AD1, BD1, and CD1).With the addition of the second dose of retardant admixtures to the third group mixtures, their initial and final setting time delayed by 13.3 %, 12.1% and 12.3 compared to initial setting time of the first group mixtures and delayed by 10.7%, 11% and 12% compared to the final setting time of the first group mixtures as shown in Fig. 7. As the general effect of retardant admixtures was to delay concrete hardening, the effect of adding the second dose of the mixtures to the mixes of the third group has continued, but with fewer rates. The results indicated that the timing of the addition of retardant admixtures half an hour before the initial set of concrete had slowed concrete hardening with fewer rates compared to the timing of the addition of the second dose of retardant admixtures after a time equal to the middle of the initial setting time. The reason for this was that the plasticity of fresh concrete had largely been lost over time and that it had not been able to recover the proper liquidity that helped to slow down the shape of concrete further. At this point, it was difficult for the concrete to absorb and interact with the admixtures, which showed that it did not have a clear effect on the slowdown of the hardening process.

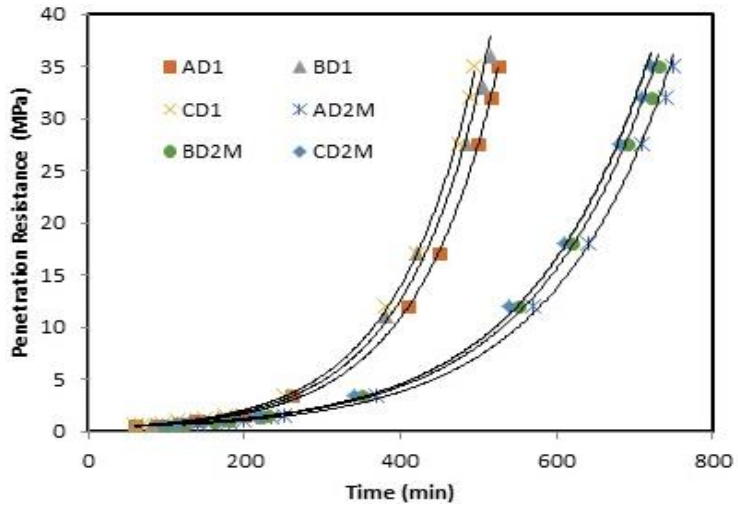

Fig. 6. Comparison between setting time values of first group mixtures and second group mixtures.

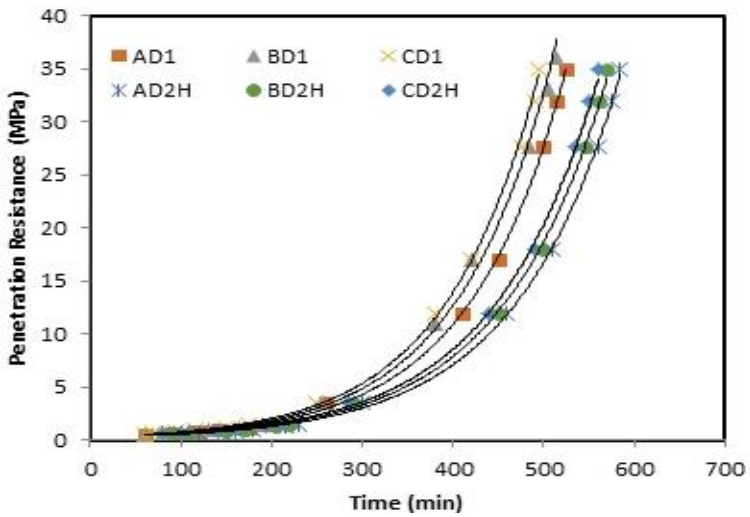

Fig. 7. Comparison between setting time values of first group mixtures and third group mixtures.

4.3. Compressive strength

Table 6 shows the compressive strength values for all samples tested at ages 7, 28, 56 and 90 days. The results illustrated a significant increase in compressive strength of the mixtures in which the retardant admixtures were used at the start of blending and at all ages for the three types of admixtures used.

Table 6. Compressive strength values for all mixtures used.

Mixes codes	Compressive Strength(MPa)			
	7 days	28 days	56 days	90 days
CN0	28	33	40	46
AD1	32	38	45	52
AD2M	29	34	39	44
AD2H	26	30	32	35
BD1	31	37	44	50
BD2M	28	33	39	43
BD2H	25	29	31	34
CD1	30	36	43	50
CD2M	27	32	38	43
CD2H	24	28	31	34

The compressive strength of all mixtures of the first group in which the retardant admixtures were used at the start of mixing exceeded the compressive strength of the control mixture at all ages. The average percentages of increasing in compressive strength were 9.7% at 7 days, 10.8% at 28 days, 9.1% at 56 days and 9.3% at 90 days than control mixture. This was due to the fact that the admixtures increased the interaction and movement of cement particles that were non-reactive at all ages (Alsadey, 2013).

Fig. 8 shows the compressive strength values for mixtures that contained first retardant admixture (AD) at different ages by displaying values at each age. It was found that the value of compressive strength increased when using the admixture (AD) at the beginning of mixing, as it improved the workability quality of the mixture, which helped to increase the compressive strength of the mixture, while when using the retardant admixture for the second time as an additional dose after the middle of the initial setting time had passed, the compressive strength value of the mixture AD2M decreased by 10.5% compared to the mixture (AD1) at 28 days of age, but its value was still higher than the compressive strength of the control mixture (CN0) by 3% at the same age.

This was because, with the passage of time, from the beginning of the mixing to the middle of the initial set time, concrete began to harden, the workability of the mixture was reduced, which was a major reason for the low compressive strength value.

When a second addition of retardant admixture was used at half an hour before the initial setting time of mixture (AD2H) occurred, it was found that compressive strength of mixture (AD2H) decreased by 21% compared to the compressive strength of mixture (AD1) and decreased by 9% compared to the compressive strength of the control mixture (CN0). It was because concrete matrix had set part of it and thus decreased rates of workability, which helped to minimize compressive strength.

The rate of increasing compressive strength for both mixtures (AD1) and (AD2M) was in the usual range for late ages (56 days and 90 days). The rate of increasing compressive strength for the mixture (AD2H) over time was sluggish, as the compressive strength value for it reached 32 N/mm² at the age of 56 days, which was expected to reach it at 28 days. This indicated that the second use of retardant admixture half an hour before the initial assumption occurred had a damaging impact because it served to decrease concrete strength.

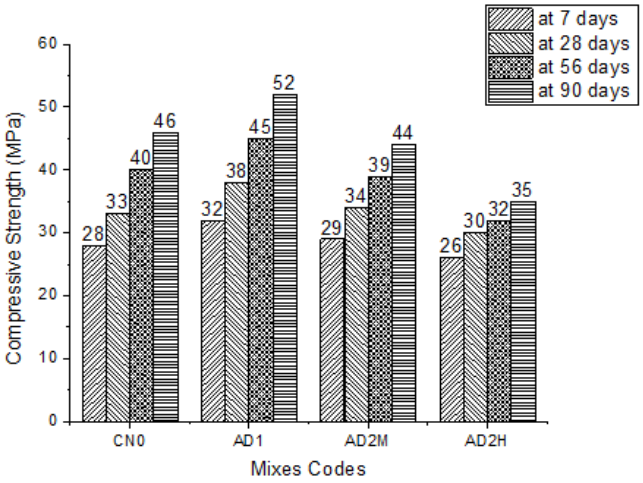

Fig. 8. Compressive strength values of first admixture mixtures (AD) comparing with compressive strength of control mixture (CN0).

Fig. 9 displays a comparison between the compressive strength value of the control mixture (CN0) at different ages and the compressive strength values when using the second admixtures (BD), whether at the start of mixing or at the middle of the calculated initial setting time or half an hour before the initial setting time has

been occurred. In the presence of the retardant admixture (BD1) at the start of batching, the compressive strength increased in all ages. The rise in compressive strength was 9.7%, 10.8%, 9%, 8% respectively at 7, 28, 56, 90 days compared to control the mixture (CN0). The compressive strength value of the mixture (BD2M) decreased by 10.8% compared to the mixture (BD1) at the age of 28 days. This was because when the retardant admixture was added for the second time in the middle of the initial setting time, it caused a delay in time that worked to allow a partial set for some concrete particles to occur. This operation helped to slow down the reaction process between water and cement particles. The slower the reaction, the lower the bonding force between the concrete particles, which reduced the compressive strength. However, it did not prohibit the maintenance of an installation, even though it was simple compressive strength, to prohibit its configuration, which could lead to disposal in the case of an emergency at the site, because the compressive strength of the mixture was still greater than the compressive strength of the control mix.

It is also clear from the figure that the compressive strength decreased by 21.6% compared to the compressive strength of (BD1) at 28 days of age when using the second dose of the mixture half an hour before the occurrence of the initial setting time which calculated in advance by the mixture penetration resistance (BD2H). This was because the reaction happened as soon as the water reached the cement granules and concrete bonds started to form, and when the admixture was used the hardening phase slowed down and the mixing state was insignificant currently, thus reduced the compressive strength. The compressive strength trend for the second admixture (BD1) at later ages was similar to the first admixture (AD1).

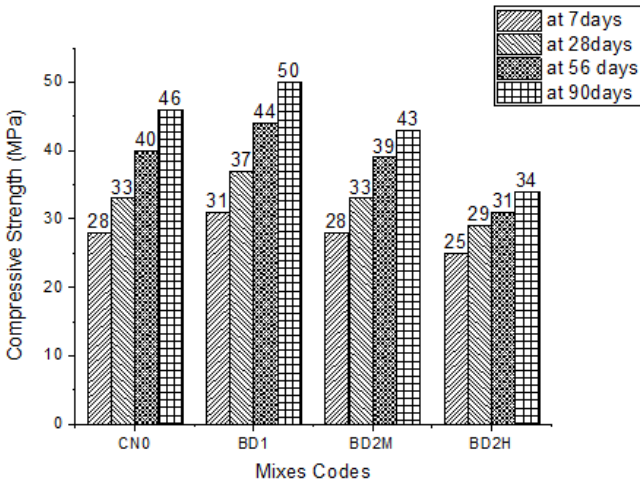

Fig. 9. Compressive strength values of second admixture mixtures (BD) comparing with compressive strength of control mixture (CN0).

Fig. 10 shows the compressive strength values for the third admixture (CD) at different ages 7, 28, 56, and 90 days and as a relationship with the compressive strength of control mixture at the same age. The compressive strength of mixture (CD1) in which the retardant admixtures were used at the start of mixing exceeded the compressive strength of the control mixture at all ages, increasing by 6.7% at 7 days, 8.3% at 28 days,7% at 56 days and 8% at 90 days. As happened with the first and second admixtures, it was found that the values of the compressive strength when using the retardant admixture during mixing process exceeded the values of compressive strength of concrete, as well as for an improvement in workability, which helped in improving compaction, which helped increase the strength of concrete.

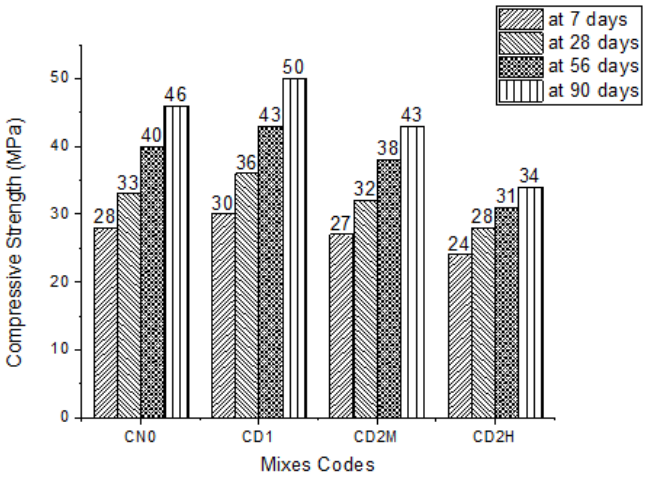

Fig. 10. Compressive strength values of third admixture mixtures (CD) comparing with compressive strength of control mixture (CN0).

In terms of the value of the resistance to compressive strength when using a second dose of admixture, the compressive strength from as it was at the start of mixing by 10% at 7 days, 11.1% at 28 days, 11.6% at 56 days and 14% at 90 days. This was due to a change in the strength of concrete, where the second addition slowed the completion of the reaction process between water with cement, which slowed hardening process. From the homogeneity of the admixture, which helped in the absence of good cohesion between the particles, and that the medium became inconsistent, and the difference between the hardening rate and its incompatibility might also be a factor in reducing compressive strength. However, the compressive strength values for this mixture (CD2M) were still higher than the compressive strength values for the control mixture (CN0); the compressive strength of the mixture was still good and appropriate given the increased initial setting time more because of the use of retardant admixture. When the second dose of the retardant admixture was used half an hour before the initial setting of the mixture was done, the compressive strength values for the mixture (CD2H) were lower than the compressive strength values of the control mixture (CN0) by 20% at 7 days, 22.2% at 28 days, 28% at 56 days and 32% at 90. That was to say, the use of retardant admixture at this period helped loosen the bonds between the concrete particles after they started to consolidate and interconnect which helped mixtures to multiply over time and was the explanation for their low compressive strength.

5. Conclusions

This paper investigates the effect of three types of retarding admixtures on the performance of concrete. The study concluded that:

- The use of an additional second dose of retardant admixtures after a time equivalent to the middle of the initial setting time helped concrete to recover its workability which facilitates the slipping of aggregates and cement granules. Slump values were increased again due to the use of an additional dose of retardant admixtures.
- The second additional dose of retarding admixtures not only delayed the concrete setting but also was effective for concrete compressive strength.
- The use of an additional second dose of the retardant admixtures after a time equivalent to the middle of the initial setting time has yielded acceptable results for the concrete properties in forms of workability and compressive strength. However, the use of the additional second dose half an hour before the initial setting time occurred has not significantly effect on concrete properties.
- The first admixture (AD) gave results better than the other two types used in this study for the properties of concrete in terms of workability, setting time and compressive strength.
- The use of an additional dose of retardant admixtures is an important option for preventing the return of ready-mixed fresh concrete and postponing casting without harmful effects by keeping the concrete in a fresh condition more than 5 h.

Acknowledgements

Thanks to the research laboratory and materials strength at the Faculty of Engineering, Menoufia University, we take this opportunity to share our deep wisdom of appreciation for presenting and completing this work. There was no exact funding in the public, commercial, or non-profit sectors to this research.

References

ACI 211.1-91 (1991). Standard Practice for Selecting Proportions for Normal, Heavyweight, and Mass. American Concrete Institute, USA.

AIshamsi AM, Alhosani KI, Yousri KM (1997). Hydrophobic materials, superplasticizer and microsilica effects on setting of cement pastes at various temperatures. *Magazine of Concrete Research*, 49(179), 111-115.

Alsadey S (2013). Effects of super plasticizing and retarding admixtures on properties of concrete. *International Conference on Innovations in Engineering and Technology*, 25-26.

ASTM C09 (2008). Standard Test Method for Time of Setting of Concrete Mixtures by Penetration Resistance. ASTM International, West Conshohocken, USA.

ASTM C143 (2015). Standard Test Method for Slump of Hydraulic Cement Concrete. ASTM International, West Conshohocken, USA.

Belous NK, Koshevar VD, Rodtsevich SP (2009). Composite retardants of hydrophobic-structuring type and their effect on properties of plasticized concretes. *Russian Journal of Applied Chemistry*, 82(9), 1669-1674.

Blankendaal T, Schuur P, Voordijk H (2014). Reducing the environmental impact of concrete and asphalt: a scenario approach. *Journal of Cleaner Production*, 66, 27-36.

Borhan TM, Al-Ramahee MA, Al-Hassnawi N, AlZaidi ZA (2018). Influence of a retarding admixture on the behavior of mortars made from different types of cement. *International Journal of Engineering & Technology*, 7(4.20), 334-337.

Brooks JJ, Johari MM, Mazloom M (2000). Effect of admixtures on the setting times of high-strength concrete. *Cement and Concrete Composites*, 22(4), 293-301.

E.S. 4765-1 (2012). Composition, Specification and Conformity Criteria of Common Cements. Egyptian Organization for Standardization and Quality Control, Egypt.

Erdoğan TY (1997). Admixtures for Concrete. Middle East Technical University, Ankara, Turkey.

Esfahani SM, Zareei SA, Madhkhan M, Ameri F, Rashidiani J, Taheri RA (2021). Mechanical and gamma-ray shielding properties and environmental benefits of concrete incorporating GGBFS and copper slag. *Journal of Building Engineering*, 33, 101615.

Fernandes A, Guptha KG (2021). Effect of modern chemical admixtures on the performance of strength of cement mortar cubes. *Advances in Civil Engineering and Infrastructural Development*, 165-173.

Ferrari G, Miyamoto M, Ferrari A (2014). New sustainable technology for recycling returned concrete. *Construction and Building Materials*, 67, 353-359.

Gebremichael NN, Karein SM, Karakouzian M, Jadidi K (2019). Investigation of setting time and compressive strength of ready-mixed concrete blended with returned fresh concrete. *Construction and Building Materials*, 197, 428-435.

Gnanaraj SC, Chokkalingam RB, LiziaThankam G (2020). Effects of admixtures on the self compacting concrete, state of the art report. *IOP Conference Series: Materials Science and Engineering*, 1006(1), 012038.

Gonzalez GP, Moo-Young HK (2004). Transportation applications of recycled concrete aggregate. *FHWA State of the Practice National Review*, 1-47.

Khan B (2004). Effect of a retarding admixture on the setting time of cement pastes in hot weather. *Engineering Sciences*, 15(1), 1319-1347.

Kubissa W, Jaskulski R, Grzelak M (2021). Torrent air permeability of concrete made with the use of air entraining agent and citric acid as setting retardant. *Construction and Building Materials*, 268, 121703.

Lee T, Lee J, Kim Y (2020). Effects of admixtures and accelerators on the development of concrete strength for horizontal form removal upon curing at 10 °C. Construction and Building Materials, 237, 117652.

Neville (2013). Properties of Concrete. 5th. ed., John Wiley & Sons, Inc., New York, NY.

Obla K, Kim H, Lobo CL (2007). Crushed returned concrete as aggregates for new concrete (No. Project 05-13). National Ready Mixed Concrete Association.

Ozturk AU, Baradan B (2011). Effects of admixture type and dosage on microstructural and mechanical properties of cement mortars. *KSCE Journal of Civil Engineering*, 15(7), 1237.

Rohden AB, Dal Molin DC, Vieira GL (2012). Time for concrete casting: a new paradigm. *Revista IBRACON de Estruturas e Materiais*, 5(6), 798-811.

Sadiqul Islam M, Tanveer Raihan M, Mehedi Hasan, Rashadin MD (2019). Effect of retarding superplasticizers on the properties of cement paste, mortar and concrete. *Asian Journal of Civil Engineering*, 20(2), 591–601.

Souza MT, Ferreira IM, de Moraes EG, Senff L, de Oliveira APN (2020). 3D printed concrete for large-scale buildings: An overview of rheology, printing parameters, chemical admixtures, reinforcements, and economic and environmental prospects. *Journal of Building Engineering*, 101833.

Suresh S, Revathi J (2016). Effect of M-sand on setting time of high performance concrete. *Asian Journal of Research in Social Sciences and Humanities*, 6(10), 1648-1654.